The Pennsylvania State University

The Graduate School

Department of Electrical Engineering

NANO-STRUCTURED TIO_2 AND APPLICATIONS TO ENERGY HARVESTING

A Dissertation in

Electrical Engineering

by

Chih-Min Lin

Submitted in Partial Fulfillment
of the Requirements
for the Degree of

Doctor of Philosophy

December 2014

The dissertation of Chih-Min Lin was reviewed and approved* by the following:

Shizhuo Yin
Professor of Electrical Engineering
Dissertation Advisor
Chair of Committee

James K. Breakall
Professor of Electrical Engineering

Julio Urbina
Associate Professor of Electrical Engineering

Qi Li
Professor of Physics

Kultegin Aydin
Head of Department

*Signatures are on file in the Graduate School

Abstract

Dye-sensitized solar cells have been developed for two decades. However, the highest light-to-electricity power conversion efficiency still remains at ~11 percent based on TiO2 nanoparticle-thin film with thickness of over 10μm for many years. One of the main issues for further enhancement of the power conversion efficiency in dye-sensitized solar cells, as the analyses of their parameters show, is the fundamental tradeoff between light-harvesting efficiency and the recombination rate in the photoelectrodes of dye-sensitized solar cells. How to develop a novel electrode to maintain a high light-harvesting efficiency and provide good charge transport properties remains a major issue.

Three-dimensional (3-D) titanium dioxide (TiO_2) nanoforests with a large surface area and high-electron transport properties have been successfully synthesized on transparent conducting oxide (TCO) substrate by using a unique multi-step hydrothermal synthesizing process. First, TiO_2 nanorods with well-controlled density and length are grown on TCO glass substrate. TiO_2 nanowires are then synthesized on TiO_2 nanorods with another hydrothermal process. In comparison with previously reported one-dimensional (1-D) TiO_2 nanorod arrays, TiO_2 nanoforests offer a larger

surface area for the same height, which is beneficial for achieving a higher-efficiency dye-sensitized solar cell (DSSC). The experimental results confirm that a conversion efficiency of 3.93 percent can be achieved with a 5.1μm long TiO_2 nanoforest-based DSSC.

According to the previous research, electrons have better charge transport ability in anatase TiO_2 than rutile TiO_2. A novel method to grow single crystal anatase TiO_2 nanowires was proposed. A bulk-like TiO_2 thin film was deposited on transparent conducting oxide (TCO) substrate to act as a protective layer of TCO substrate and a starting material for hydrothermal synthesis in a strong alkaline solution (10M NaOH). After the hydrothermal process, $Na_2Ti_3O_7$ nanowires were synthesized on TCO substrate. Single crystal anatase nanowires were successfully synthesized on TCO substrate after ion exchange and annealing. The light-to-electricity conversion efficiency of DSSCs based on $2.2\ \mu m$ anatase nanowires reaches 5.2 percent, which was the highest efficiency of single crystal anatase TiO_2 nanowire-based DSSCs realized in early 2012.

TABLE OF CONTENTS

LIST OF FIGURES

LIST OF TABLES

Acknowledgements

I would like to express the deepest gratitude to my advisor, Prof. Shizhuo Yin, for his continuous support and guidance. He offered me help when I most needed it in the course of my graduate career. His enthusiasm and engagement have been an inspiration for me. His patience and trust have allowed me to learn and grow in this profession, trying out different ideas and methods. I am grateful that he was always there to offer help and advice, especially when I encountered difficulties in my research. Without his persistent guidance and generous support, this thesis would not have been possible.

I would also like to thank Prof. Breakall, Prof. Urbina, and Prof. Li for their insights on and suggestions for the development of my project and their generous encouragement in my comprehensive exam.

Special thanks are due to my group members, Yun-Ching, Chao, and Jimmy, with whom I have shared a history of hard work and challenging moments. We brainstormed and exchanged research ideas and supported each other. The research would not have gone that well without them.

I am particularly grateful to Prof. Yin, who supplied intellectual guidance and financial support for my graduate life. The financial support that he offered allowed me

to pursue this project.

Lastly, I would like to thank my wife, Grace, my family, and my friends for everything they did. Without their love and support, this journey would definitely have been more difficult. I am so lucky to have them.

Chapter 1
Introduction

1.1 Development of renewable energy

In recent years, the price of fossil fuels remains high because of the expectation of fossil resource shortage. Moreover, increasing greenhouse gas emissions generated by burning fossil fuels have caused global warming effects, including climate change and extreme weather. The cost of fuels and the impact of fuel consumptions on the environment and on climate change have stimulated much more investment in developing forms of renewable energy. These forms of renewable energy include solar hot water, geothermal power, hydropower, biodiesel, wind power, solar photovoltaic devices, and concentrated solar power (CSP). In 2011, renewable energy reached 9 percent of total global energy [1.1].

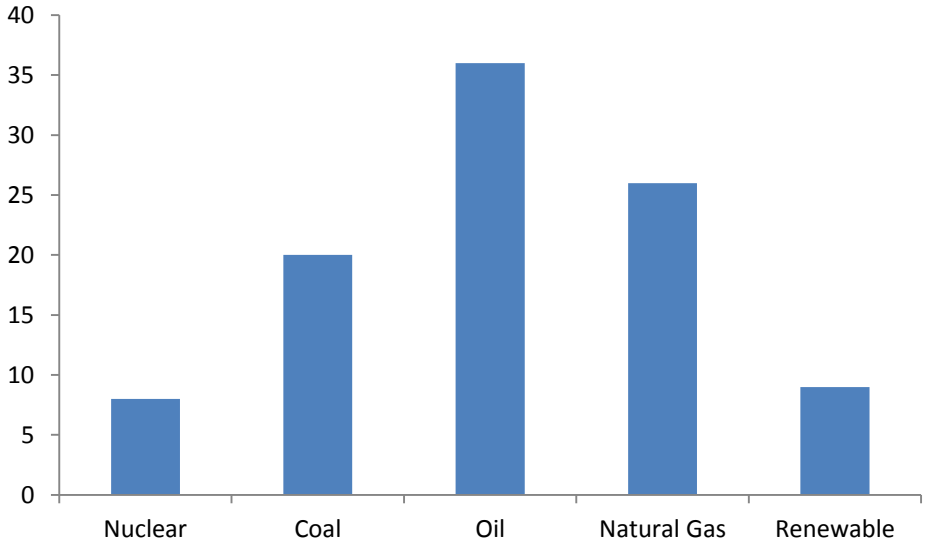

Figure 1-1 Share of different energy resources in 2011

Each form of renewable energy has its advantages and disadvantages (see Table 1). Among the variety of renewable energy technologies, power generated from solar photovoltaic devices has had the highest growth rate in recent years because of the practical demand (e.g. portable applications) and the rapid development of technologies (solar cells of different generations) [1.2].

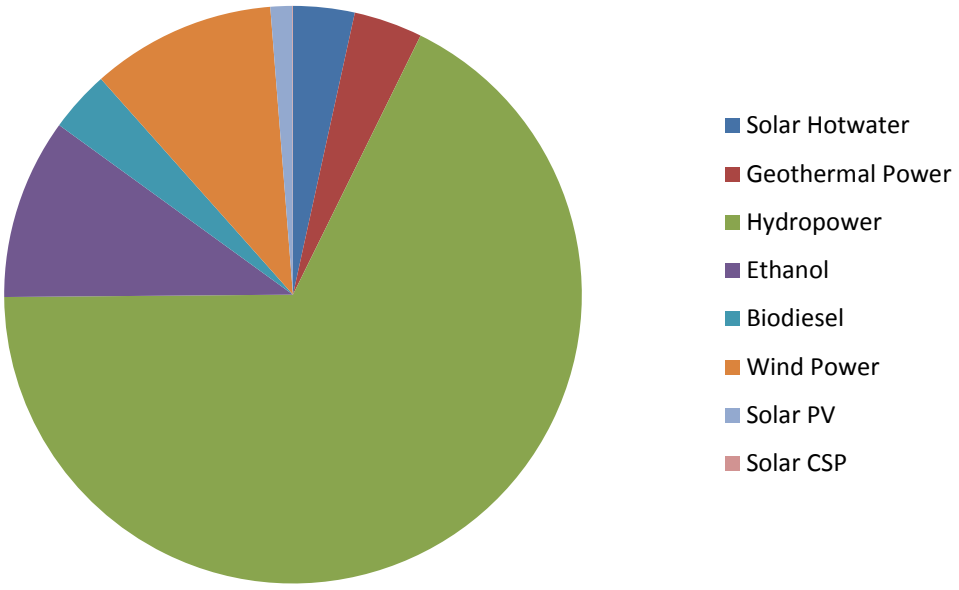

Figure 1-2 Share of different renewable energy resources in 2011

	Advantage	Disadvantage
Solar hotwater	• infinite source • clean	• Dependent on the weather • high upfront cost
Geothermal power	• infinite source • clean • reliable source of energy • minimal land	• Not many spaces • high upfront cost
Hydropower	• infinite source • clean	• migration of fish • affected by the weather(e.g. drought) • impact on the environment(e.g. natural habitat of some living)

Ethanol	• plant-based fuel produced from sources (sugar cane, corn, waste paper, grains, and etc) • clean	• need of land may restrict other uses (e.g. animal feed) • frequent engine maintenance because ethanol can easily absorb water and dust)
Biodiesel	• many sources(e.g. crop waste, manure, and other byproducts) • lower carbon emission	• cannot be directly used • storage • production of biodiesel may affect production of food
Wind Power	• infinite source • clean	• Not reliable source of energy • noisy
Solar PV	• infinite source • clean	• dependent on the weather • expensive
Solar CSP	• infinite source • clean	• expensive • not reliable source of energy

Table 1-1 Comparisons of different types of renewable energies

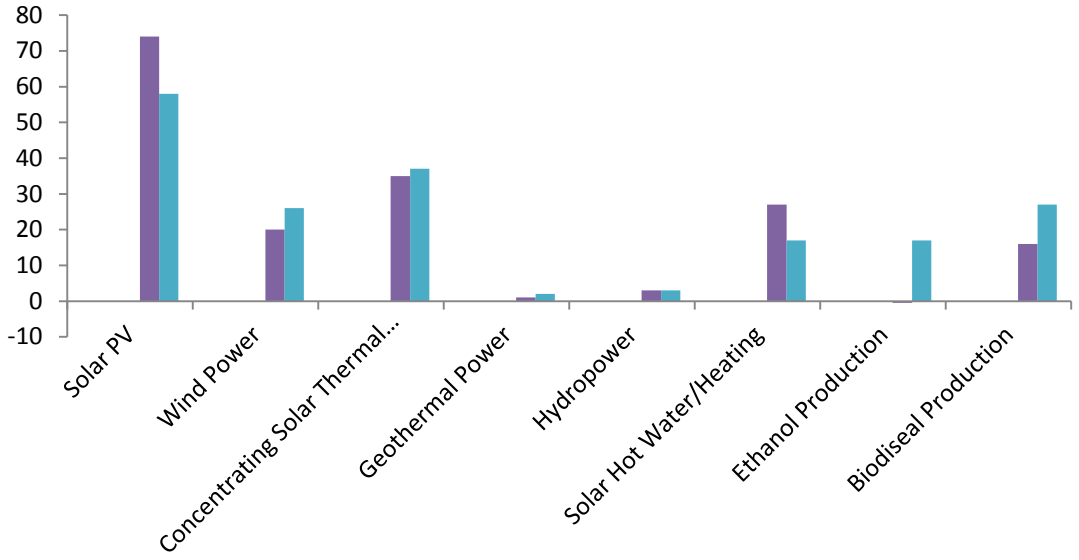

Figure 1-3 Growth rates of different renewable energies. The purple bar shows the growth rate in 2011. The blue bar represents the average growth rate from 2006 to 2011.

1.2 Solar cells of different generations

1.2.1 First generation:

First-generation solar cells are usually described as single-crystal or poly-crystal silicon-based solar cells. The major advantage of first-generation solar cells is high power conversion efficiency. The highest efficiency of single-crystal silicon based solar cells is around 24 percent. However, the worst drawback is its high cost; the price of silicon-based solar cells is usually determined by the price of single-crystal and poly-crystal silicon. Even though the price is high, first-generation solar cells are still the primary product for current commercial solar cells due to their high stability and

matured technology [1.3-1.4].

1.2.2 Second generation:

Second-generation solar cells are also called thin-film solar cells because the thickness of the devices can be reduced to several micrometers, much thinner than silicon-based solar cells. Thin-film solar cells were developed to reduce the fabrication cost and need for source materials (e.g. single-crystal and poly-crystal silicon) of first-generation solar cells. Second-generation solar cells are usually fabricated by deposition technology (e.g. chemical vapor deposition). Types of second-generation solar cells include amorphous silicon thin-film solar cells, cadmium telluride (CdTe), copper indium selenide (CIS), and copper indium gallium selenide (CIGS) solar cells. The advantage of using second-generation solar cells is their relatively low cost of fabrication, reducing the quantity of source materials used in fabricating solar cells. The disadvantages of thin-film solar cells are the following: a) the toxic byproducts may pollute the environment; b) the power conversion efficiency of thin-film solar cells is still low due to the complexity of fabrication technology [1.5-1.7].

1.2.3 Third generation:

Third-generation solar cells are made from a variety of new materials, including

nanotubes, nanowires, other nanostructured materials, organic dyes, and conductive plastics. The development of third-generation solar cells aims at increasing the light absorption spectrum (e.g. infrared (IR) region) of the active materials of solar cells, reducing the fabrication cost, and developing more uses in daily life. Examples of third-generation solar cells include nanocrystal-based solar cells, polymer-based solar cells, dye-sensitized solar cells, and concentrated solar cells [1.8-1.10].

As technologies have created different types of solar cells, many applications have been developed, such as transparent solar glass, solar buses, solar ships, and portable electronic devices. Not all types of solar cells and their applications are matured. Solar cells of different technologies have their limitations or restrictions on applications. For example, single-crystal silicon-based solar cells may not be ideal for portable electronic devices because a) the power conversion efficiency is very low because the indoor light spectrum differs from the sunlight spectrum; b) silicon-based solar cells are relatively larger and heavier than second-generation and third-generation solar cells.

Among these varieties of solar cells, this research focuses on dye-sensitized solar cells for the following reasons [1.11-1.13].

1. Low fabrication costs: dye-sensitized solar cells are fabricated at low temperatures

and can be fabricated in a non-cleanroom environment.

2. Development of nanotechnology: metal oxide nanostructures (e.g. nanoparticles, one-dimensional structures, and three-dimensional structures) with large surface areas were developed in recent years. These structures as developed can be adopted as n-type photoelectrodes in dye-sensitized solar cells.

3. Wider light absorption spectrum: in contrast to other solar cells, the absorption spectrum of dye, which is a photon sensitizer, can be modulated through different chemical syntheses so that the dye-sensitized solar cells will have a wider light absorption spectrum. With this property, dye-sensitized solar cells can be potentially adopted for more applications, especially for portable devices. **Fig. 1-4** shows the diagram of a dye-sensitized solar cell.

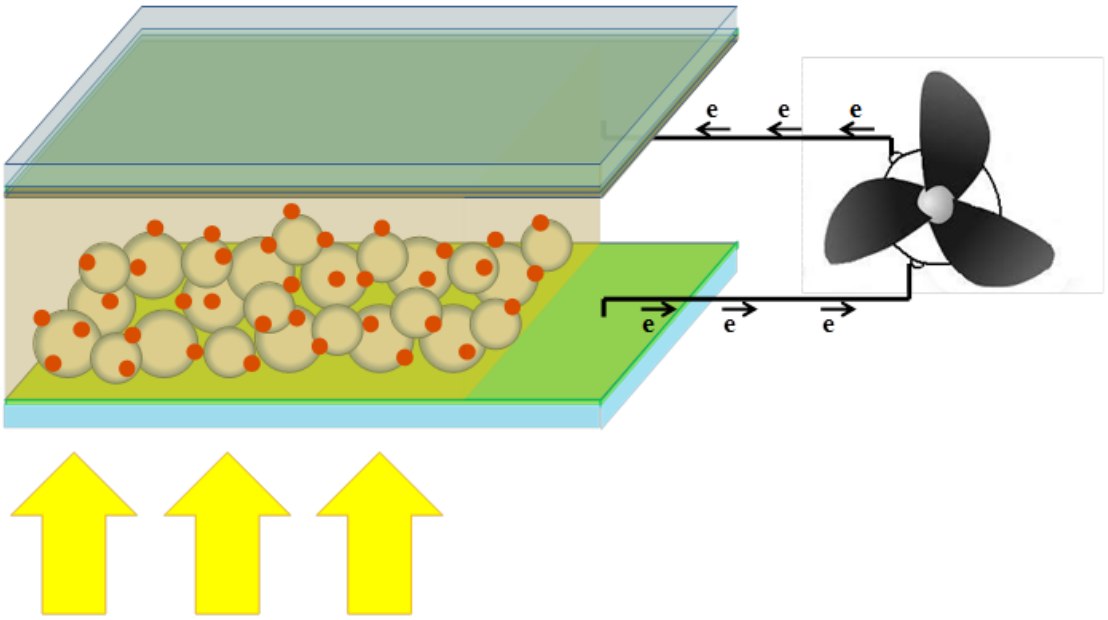

Figure 1-4 The diagram of a dye-sensitized solar cell

1.3 Nanostructured TiO_2 for Dye-Sensitized Solar Cells

Nanostructured semiconductors play an important role in the transition from traditional fossil energy to renewable energy and accelerate the utilization of sunlight. For example, the properties of high surface area to volume ratio and good conductivity of nanostructured metal oxides elevate the efficiency of dye-sensitized solar cells or water-splitting devices. These semiconductors are usually metal oxides, such as TiO_2, ZnO, and SnO_2 [1.30-1.32]. Among these materials, titanium dioxide attracts the most attention for the development of dye-sensitized solar cells because of the following properties:

a. TiO_2 is highly transparent to visible light. The band gap of TiO_2 is around 3.2ev, which makes TiO_2 a good material to use as a photoelectrode in a dye-sensitized solar cell.

b. TiO_2 is a chemically stable material. Excited electrons are usually injected into TiO_2 from dyes via hydrogen or chemical bonding. (The details will be discussed in Chapter Two.) This chemical stability ensures that no chemical reaction happens between the TiO_2 and the dye, so that electrons can be efficiently injected into the conduction band of TiO_2.

c. TiO_2 is an abundant material. The cost to derive it is very low.

d. The band position of TiO_2 makes it a good n-type semiconductor material for use in photoelectrodes when it is applied to dye-sensitized solar cells. The energy level of the conduction band is slightly lower than the lowest unoccupied molecular orbital (LUMO) of dyes, meaning that 1) electrons can easily be injected into TiO_2 from dyes and 2) large open circuit voltage can be derived.

e. TiO_2 has good conductivity properties.

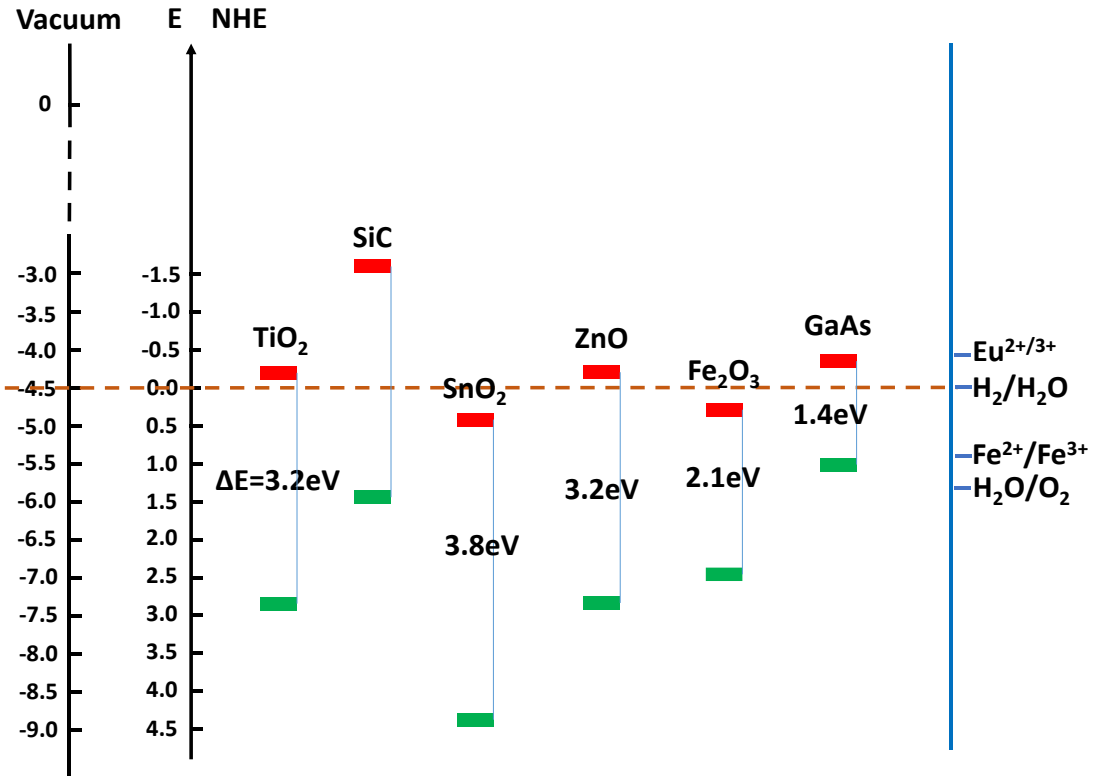

Figure 1-5 Band positions of different semiconductors. The red bars represent the conduction bands of the semiconductors, and the green bars represent the conduction bands of the semiconductors [1.14].

1.3.1 Different phases of TiO_2

TiO_2 basically has three common phases: rutile (tetragonal) anatase (tetragonal), and brookite (orthorhombic). Of these three phases, rutile (see **Fig. 1-6**) and anatase (see **Fig. 1-7**) have better applications. Rutile is the most stable. Anatase can provide the best charge transport properties. The high reflective index (n) makes TiO_2 a good

material to use for an anti-reflection layer (n of anatase is 2.488, and n of rutile is 2.609).

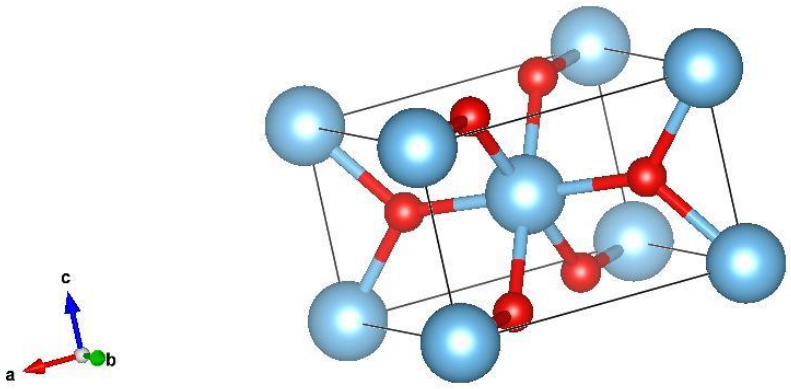

Figure 1-6 The crystal structure of rutile. The blue balls represent titanium atoms, while red balls represent oxygen atoms.

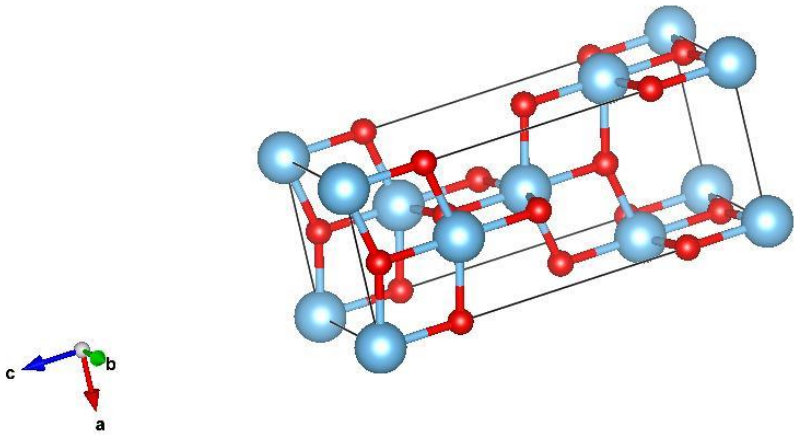

Figure 1-7 The crystal structure of anatase. The blue balls represent titanium atoms, while red balls represent oxygen atoms.

1.3.2 Different morphologies of TiO_2:

a. Nanoparticles:

A nanoparticle has the simplest morphology of any nanostructure. The sol-gel method is usually used for nanoparticle synthesis. To synthesize TiO_2 nanoparticles, a titanium precursor (i.e., titanium (IV) isopropoxide (TTIP)) is dissolved in a mixture of de-ionized (DI) water, ethanol, and nitric acid. After being stirred for half an hour, the solution is aged for 24 hours to form gel. After drying and annealing this gel, TiO_2 nanoparticles can be derived [1.15-1.16].

One of the main advantages of TiO_2 nanoparticles is that the method to synthesize nanoparticles is relatively easy. The other is that TiO_2 nanoparticles can be easily synthesized on substrates (transparent conducting oxide or flexible substrate) by blade paste method when they are used on some applications (e.g. solar cells and water-splitting devices). The disadvantage of nanoparticles is that the electron properties are relatively lower than those of one-dimensional or three-dimensional single crystal nanostructures.

b. One-dimensional TiO_2:

One-dimensional TiO_2 nanostructures were developed to provide shorter electron transport pathways than TiO_2 nanoparticles. There are several one-dimensional TiO_2 nanostructures which can be synthesized by different methods. Two representative TiO_2 one-dimensional nanostructures, nanotubes and nanowires, will be introduced below:

i. Nanotubes:

TiO_2 nanotubes can be synthesized by several methods:

(a) Electrochemical anodization method: the anodization method is the commonest method used to synthesize TiO_2 nanotubes on titanium or fluorine-doped tin oxide (FTO) substrate [1.17-1.18]. By oxidation of the titanium and dissolution of the titanium dioxide by the fluorine ions in the electrolyte, well-aligned TiO_2 nanotubes gradually form and grow on the substrate (see **Fig. 1-8**). The dimensions, including wall thickness, length of nanotube, and inner and outer diameters, can be controlled by the electrolyte, time, and operational voltage.

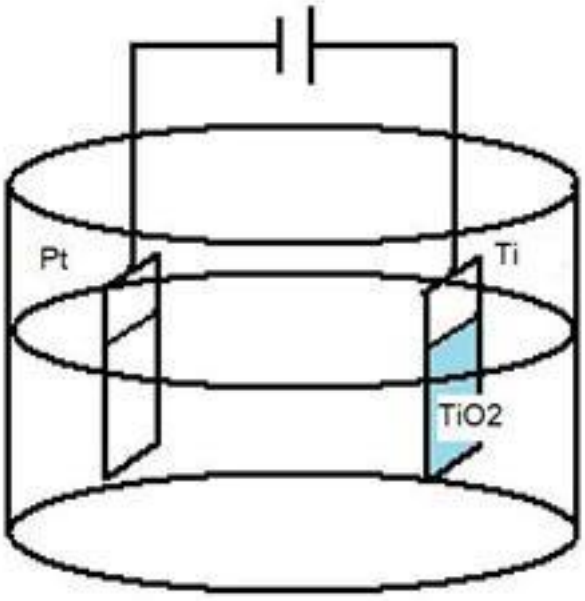

Figure 1-8 Experimental setup of the anodization method: Ti acts as the anode, and the platinum foil acts as a cathode. The experiment is conducted in an electrolyte containing fluorine ions at room temperature.

(b) Template-assisted method: Anodic aluminum oxide (AAO) is usually used as a template to synthesize nanotubes or nanowires by electro-deposition or the sol-gel process. After nanotubes or nanowires form in the pores of the AAO, it is removed in a base solution (NaOH aqueous solution) [1.19-1.21]. The advantage of the template-assisted method is that the morphology can be well controlled with different templates. However, the drawback is the

high cost of the template, so this method is often too expensive to be applied to fabrication of TiO_2 nanostructures.

The advantages of TiO_2 nanotubes are 1) this structure can provide a direct charge transport pathway for electrons, so that the transport distance will be much shorter than in a nanoparticle-composited structure and 2) a TiO_2 nanotube structure can provide a large surface area by controlling the dimension of the structure for many applications (e.g. dye-sensitized solar cells, photocatalysts, and gas sensing). However, this structure also has its drawbacks. The main problem is crystallization. A single-crystal nanotube cannot be synthesized using the anodization method. Therefore, the electron transport properties in this structure will not be as good as expected due to the traps at the surfaces of the polycrystals.

ii. Nanowires:

TiO_2 nanowires can be synthesized by the following methods:

(a) Hydrothermal and solvothermal methods: Hydrothermal and solvothermal methods are techniques used to synthesize crystal materials from high-temperature solutions at high vapor pressures [1.22-1.24]. The difference between hydrothermal synthesis and solvothermal synthesis is the type of solvent used (e.g. the hydrothermal method is conducted in an aqueous solution, and the solvothermal method is conducted in a solution containing no water). Hydrothermal and solvothermal methods can control the size, morphology, and crystallization of nanostructures. By changing the parameters, which include time, temperature, solvents, substrates, and precursors, nanostructures can be synthesized as designed in the experiments. (see **Fig. 1-9**)

Figure 1-9 Hydrothermal/solvothermal methods are conducted in ovens. A Teflon reactor which contains precursor solution and substrates is sealed in a metal bomb.

The advantage of nanowires synthesized by hydrothermal/solvothermal methods is that such nanowires have excellent electron transport abilities with their single crystal properties and direct charge transport pathways. However, the

major disadvantage of nanowire at this stage of development is the limitation of the surface area. The dimension of TiO_2 nanowire synthesized on transparent conducting oxide (TCO) substrates cannot be well controlled when compared to TiO_2 nanotubes. For example, the maximum length of TiO_2 nanowires synthesized on TCO substrates is less than 10μm, which is much shorter than nanotubes synthesized on TCO substrates.

(b) The dimension and density of TiO_2 nanowires can also be well controlled by other synthesis methods, such as vapor–liquid–solid chemical vapor deposition (VLSCVD) and the template-assisted method. However, these fabrication techniques are expensive and do not meet the low-cost goal [1.25-1.26].

iii. Other TiO_2 nanostructures, including nanoflakes, nanobelts, pyramid-shaped nanocrystals, etc., can be synthesized via various methods, but these practical applications still cannot compete with the above structures, such as nanoparticles, nanotubes, and nanowires [1.27-

1.29].

1.4 Thesis overview

The development of TiO_2 nanostructures diversified in the past decade. Some newly-developed TiO_2 nanostructures inspired the research being examined here, and made big contributions to increasing the power conversion efficiency of dye-sensitized solar cells as well. Some of them were novel but not practical. This research focuses on the synthesis of TiO_2 nanostructures on transparent conducting oxide (TCO) substrates for better applications on dye-sensitized solar cells using low-cost methods.

The second chapter will introduce the mechanism of dye-sensitized solar cells, analyze the problems to be overcome, and explain the motivation for this research.

The third chapter will propose a novel method to synthesize three-dimensional TiO_2 nanoforests on transparent conducting oxide substrate and its application on DSSCs.

The fourth chapter will discuss the synthesis of single-crystal anatase nanowires on transparent conducting oxide substrate by a unique method not previously described.

The conclusion will present the findings of the dissertation and discuss future work to be developed on the basis of these TiO_2 nanostructures.

1.5 References

1.1. U.S. Department of Energy (DOE), Energy Information Administration (EIA) (2012) Annual Energy Review 2011.

1.2. REN 21 Steering Committee, REN21, Renewable 2013 Global Status Report

1.3. J. Zhao, A. Wang, M. a. Green, and F. Ferrazza, "19.8% Efficient 'Honeycomb' Textured Multicrystalline and 24.4% Monocrystalline Silicon Solar Cells," *Appl. Phys. Lett.*, vol. 73, no. 14, p. 1991, 1998.

1.4. D. S. Kim, A. M. Gabor, V. Yelundur, A. D. Upadhyaya, V. Meemongkolkiat, and A. Rohatgi, "STRING RIBBON SILICON SOLAR CELLS WITH 17.8 % EFFICIENCY," pp. 8–11.

1.5. X. Wu, R. G. Dhere, D. S. Albin, T. A. Gessert, C. Dehart, J. C. Keane, A. Duda, T. J. Coutts, S. Asher, D. H. Levi, H. R. Moutinho, Y. Yan, T. Moriarty, S. Johnston, K. Emery, and P. Sheldon, "High-Efficiency CTO / ZTO / CdS / CdTe Polycrystalline Thin-Film Solar Cells," no. October, 2001.

1.6. I. Repins, M. A. Contreras, B. Egaas, C. Dehart, J. Scharf, and C. L. Perkins, "19 Á 9 % -efficient ZnO / CdS / CuInGaSe 2 Solar Cell with 81 Á 2 % Fill Factor z," no. February, pp. 235–239, 2008.

1.7. J. Steinhauser, M. Marmelo, G. Monteduro, L. Castens, O. S. S. A. Neuchâtel, and C.- Neuchâtel, “High-efficiency amorphous silicon devices on lpcvd-zno tco prepared in industrial kai,” no. September, pp. 21–25, 2009.

1.8. “Development of Next Generation Organic Solar Cell,” pp. 1–12, 2010.

1.9. “Outlook Brightens for Plastic Solar Cells,” p. 30.

1.10. A. Hagfeldt, G. Boschloo, L. Sun, L. Kloo, and H. Pettersson, “Dye-sensitized solar cells.,” *Chem. Rev.*, vol. 110, no. 11, pp. 6595–663, Nov. 2010.

1.11. M. Grätzel, “Dye-sensitized solar cells,” *J. Photochem. Photobiol. C Photochem. Rev.*, vol. 4, no. 2, pp. 145–153, Oct. 2003.

1.12. Y. Chiba, A. Islam, Y. Watanabe, R. Komiya, N. Koide, and L. Han, “Dye-Sensitized Solar Cells with Conversion Efficiency of 11.1%,” *Jpn. J. Appl. Phys.*, vol. 45, no. No. 25, pp. L638–L640, Jun. 2006.

1.13. Brain O’Regan & Michael Grätzel, “A low-cost, high-efficiency solar cell based on dye-sensitized colloidal TiO_2 films,” vol. 353, p. 737, 1991.

1.14. M. Grätzel, “Photoelectrochemical cells,” vol. 414, no. November, 2001.

1.15. T. P. Chou, Q. Zhang, B. Russo, G. E. Fryxell, G. Cao, M. Science, V. Uni, and R. Hall, “Titania Particle Size Effect on the Overall Performance of Dye-

Sensitized Solar Cells," *J. Phys. Chem. C*, no. Iv, pp. 6296–6302, 2007.

1.16. R. Vijayalakshmi and V. Rajendran, "Synthesis and characterization of nano-TiO_2 via different methods," vol. 4, no. 2, pp. 1183–1190, 2012.

1.17. O. K. Varghese, M. Paulose, and C. a Grimes, "Long vertically aligned titania nanotubes on transparent conducting oxide for highly efficient solar cells.," *Nat. Nanotechnol.*, vol. 4, no. 9, pp. 592–7, Sep. 2009.

1.18. M. Ye, X. Xin, C. Lin, and Z. Lin, "High Efficiency Dye-Sensitized Solar Cells Based on Hierarchically," 2011.

1.19. L. Yuan, S. Meng, Y. Zhou, and Z. Yue, "Controlled synthesis of anatase TiO_2 nanotube and nanowire arrays via AAO template-based hydrolysis," *J. Mater. Chem. A*, vol. 1, no. 7, p. 2552, 2013.

1.20. J. J. Hill, S. P. Cotton, and K. J. Ziegler, "Alignment and Morphology Control of Ordered Mesoporous Silicas in Anodic Aluminum Oxide Channels by Electrophoretic Deposition," *Chem. Mater.*, vol. 21, no. 9, pp. 1841–1846, May 2009.

1.21. S. J. Limmer, S. Seraji, Y. Wu, T. P. Chou, C. Nguyen, and G. Z. Cao, "Template-Based Growth of Various Oxide Nanorods by Sol–Gel

Electrophoresis," *Adv. Funct. Mater.*, vol. 12, no. 1, p. 59, Jan. 2002.

1.22. B. Liu and E. S. Aydil, "Growth of oriented single-crystalline rutile TiO(2) nanorods on transparent conducting substrates for dye-sensitized solar cells.," *J. Am. Chem. Soc.*, vol. 131, no. 11, pp. 3985–90, Mar. 2009.

1.23. X. Feng, K. Shankar, O. K. Varghese, M. Paulose, T. J. Latempa, and C. a Grimes, "Vertically aligned single crystal TiO_2 nanowire arrays grown directly on transparent conducting oxide coated glass: synthesis details and applications.," *Nano Lett.*, vol. 8, no. 11, pp. 3781–6, Nov. 2008.

1.24. A. Kumar, A. R. Madaria, and C. Zhou, "Growth of Aligned Single-Crystalline Rutile TiO 2 Nanowires on Arbitrary Substrates and Their Application in Dye-Sensitized Solar Cells," pp. 7787–7792, 2010.

1.25. Z. Miao, D. Xu, J. Ouyang, G. Guo, and X. Zhao, "Electrochemically Induced Sol − Gel Preparation of Single-Crystalline TiO 2 Nanowires," 2002.

1.26. M. Okumura, S. Nakamura, S. Tsubota, T. Nakamura, and M. Azuma, "Chemical vapor deposition of gold on Al 2 O 3 , SiO 2 , and TiO 2 for the oxidation of CO and of H 2," vol. 51, pp. 53–58, 1998.

1.27. W. Ho, J. C. Yu, and J. Yu, "Photocatalytic TiO_2/glass nanoflake array films.,"

Langmuir, vol. 21, no. 8, pp. 3486–92, Apr. 2005.

1.28. H. Zhang, X. Liu, Y. Wang, P. Liu, W. Cai, G. Zhu, H. Yang, and H. Zhao, "Rutile TiO_2 films with 100% exposed pyramid-shaped (111) surface: photoelectron transport properties under UV and visible light irradiation," *J. Mater. Chem. A*, vol. 1, no. 7, p. 2646, 2013.

1.29. W. Zhou, G. Du, P. Hu, G. Li, D. Wang, H. Liu, J. Wang, R. I. Boughton, D. Liu, and H. Jiang, "Nanoheterostructures on TiO_2 nanobelts achieved by acid hydrothermal method with enhanced photocatalytic and gas sensitive performance," *J. Mater. Chem.*, vol. 21, no. 22, p. 7937, 2011.

1.30. M. Saito and S. Fujihara, "Large photocurrent generation in dye-sensitized ZnO solar cells," *Energy Environ. Sci.*, vol. 1, no. 2, p. 280, 2008.

1.31. S. Ferrere, A. Zaban, and B. A. Gregg, "Dye Sensitization of Nanocrystalline Tin Oxide by Perylene Derivatives," *J. Phys. Chem. B*, vol. 5647, no. 97, pp. 4490–4493, 1997.

1.32. Z.-S. Wang, H. Kawauchi, T. Kashima, and H. Arakawa, "Significant influence of TiO2 photoelectrode morphology on the energy conversion efficiency of N719 dye-sensitized solar cell," *Coord. Chem. Rev.*, vol. 248, no. 13–14, pp.

1381–1389, Jul. 2004.

Chpater 2
Dye-Sensitized Solar Cells

2.1 History of dye-sensitized solar cells (DSSCs)

The dye-sensitized solar cell was invented by Michael Gratzel in 1991 [2.1]. This solar cell has attracted much attention because of its relatively low fabrication cost (i.e., no cleanroom facilities and no vacuum chambers are needed), non-toxicity, and plenty of resource materials (e.g. titanium dioxide, zinc oxide, and tin oxide). However, DSSCs still have some challenges to be overcome, such as stability problems, sealing, and area limitations. The highest power conversion efficiency reported is ~11 percent, but its efficiency is still lower than other commercial solar cells, such as silicon-based solar cells or thin-film solar cells (e.g. the power conversion efficiency of the commercial single-crystal solar cells is ~20 per cent, and the power conversion efficiency of CdTe thin-film solar cells is ~14 percent) [2.2-2.3]. However, the price/performance ratio of DSSCs is low enough to compete with fossil-fuel-generated power. Many researchers have devoted themselves to improving the power conversion efficiency and making DSSCs more feasible for more applications. **Fig. 2-1** shows the

schematic of a DSSC.

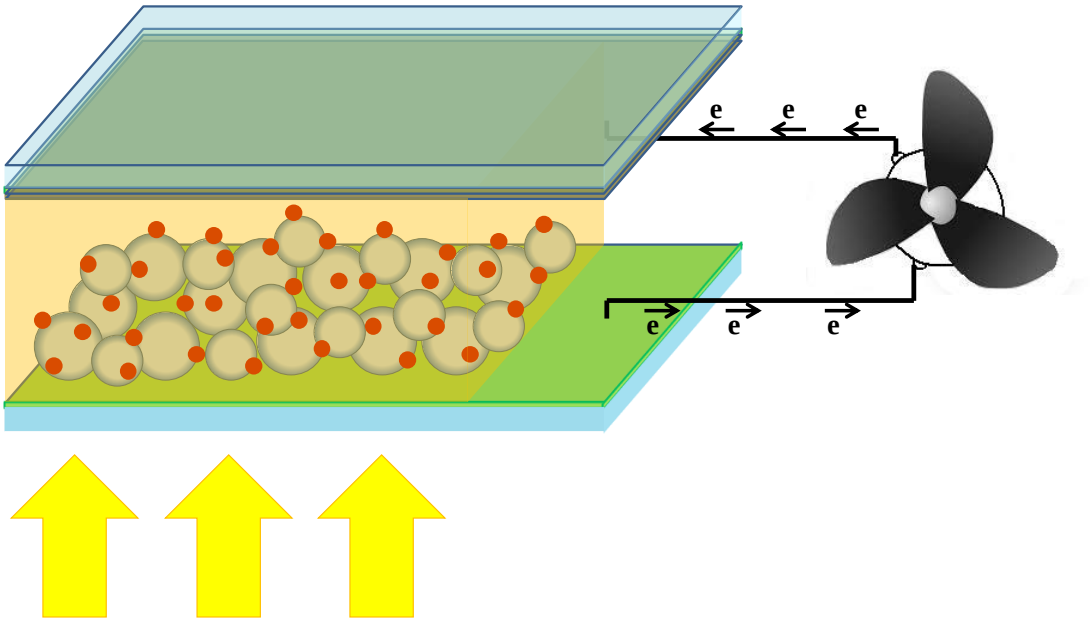

Figure 2-1 Schematic of a typical nanoparticle-based DSSC

2.2 Mechanism of dye-sensitized solar cells

To further understand the mechanism of a DSSC, the structure of a DSSC is shown in **Fig. 2-2.** DSSC was first realized as liquid DSSC. Liquid DSSC is composed of three parts: (1) the first part is n-type semiconductor material (photoanode or photoelectrode). Titanium dioxide (TiO_2) is the commonest material used for the n-type material because it has better band positions with respect to dyes, transparency to the visible light, and chemical stability. (2) The second part is dye, which is a photon sensitizer. Dyes can be

absorbed on a TiO2 surface in two ways. One is by physical absorption, such as hydrogen bonding. The other is by chemical bond formation with a unidentate linkage, a bidentate linkage, or a bridging linkage (see **Fig. 2-3**) [2.16-2.18]. (3) The third part is an electrolyte, which contains reduction/oxidation (redox) couples. Iodide ions (I^-) and tri-iodide ions (I_3^-) are usually adopted as redox couples. The power-generation cycle can be activated by the incident light (photons). When a photon excites the dye, the electron set in the highest occupied molecular orbital (HOMO) level will receive energy from the incident photon ($h\nu$) and then jump to the lowest unoccupied molecular orbital (LUMO) level of the dye.

$$S^0 + h\nu \rightarrow S^*$$

The electron set in the LUMO level will be injected into the conduction band of an n-type semiconductor (TiO_2). This action leads the dye to be oxidized.

$$S^* \rightarrow S^+ + e^-(TiO_2)$$

The iodide ion in the redox electrolyte will then reduce the oxidized dye to the original state dye, which is capable of capturing photons again. At the same time, the iodide ion is oxidized to the tri-iodide ion.

$$2S^+ + 3I^- \rightarrow 2S^0 + I_3^-$$

The tri-iodide ion will get an electron from the counter electrode and then be reduced to an iodide ion again.

$$I_3^- + 2e^-(Pt) \rightarrow 3I^-$$

Power will be generated after the generated electrons complete a transportation cycle in the external circuit pathway.

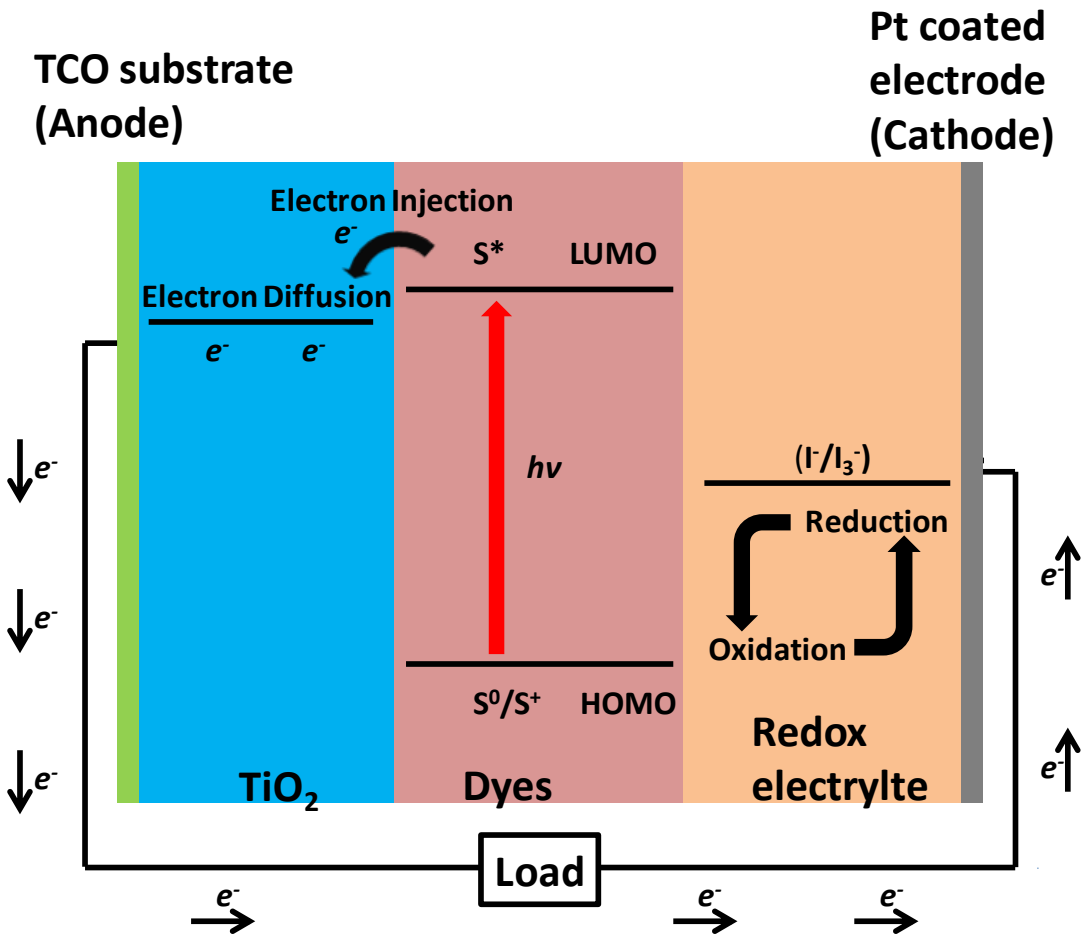

Figure 2-2 mechanism of liquid electrolyte-based dye-sensitized solar cells

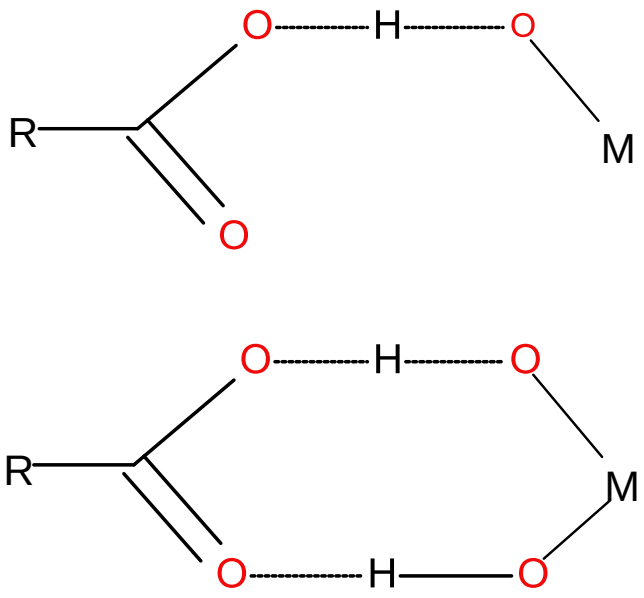

(a)

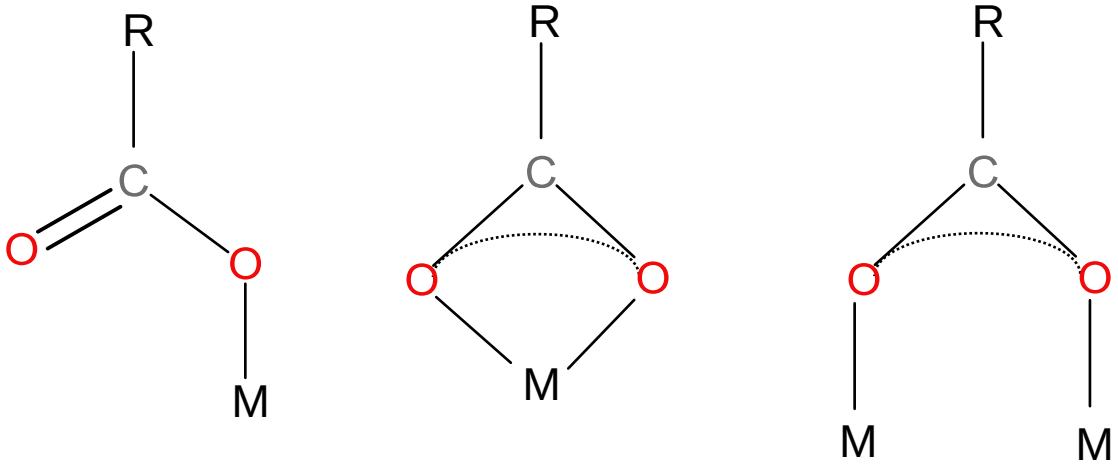

(b)

Figure 2-3 Dyes are absorbed on the surface of TiO_2 in two ways: (a) physical absorption: hydrogen bonding and (b) chemical absorption: unidentate linkage, bidentate linkage, or bridging linkage (from the left-hand side to the right-hand side)

Parameters of Dye-Sensitized Solar Cells

a. Open circuit voltage (Voc):

When the two terminals of the solar cell are floated under illumination, the voltage across these two terminals is open circuit voltage. Open circuit voltage is the optical bandgap minus the loss-in-potential [2.4]. Loss-in-potential is mainly composed of two parts. One is the driving force for the charge to be injected from the oxidized dye to the conduction band of the semiconductor (usually 100-200mV). The other is the loss caused by the energy mismatch between the oxidized dye and the Nernst potential of the redox electrolyte (usually 650mV).

b. Short-circuit current (Isc):

Short-circuit current is the current when the load resistance is 0 under illumination. There are two ways to improve the short-circuit current. One is to increase the overlap of dye absorption spectrum and solar spectrum. Some groups endeavor to develop dye sensitizers with wider spectra, containing IR or NIR regions [2.5-2.8]. The other method is to increase the absorption surface area of dyes by increasing the thickness of the sensitized nanostructured thin film. The drawback of the latter method is that the

short-circuit current is considerably affected by the charge-diffusion length in the nano-structured thin film. 1-D morphology is known to have at least one order longer diffusion length than this particular morphology, and this is why many groups focus on developing 1-D-structured thin film in recent years [2.9-2.10].

c. Fill Factor(*FF*):

Fill factor is defined as follows: (see **Fig. 2-4**)

$$FF = \frac{P_m}{V_{oc} \times I_{sc}} \qquad (2.1)$$

where P_m is the maximum power output.

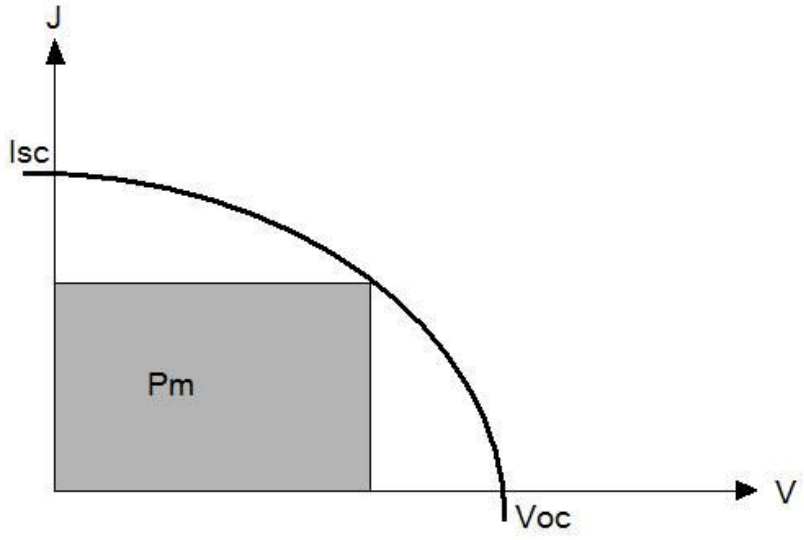

Figure 2-4 J-V curve of dye-sensitized solar cell

FF is determined by the series resistance (R_S) and shunt resistance (R_{SH}) of the solar cells. An equivalent circuit of solar cells is shown in **Fig. 2-5**.

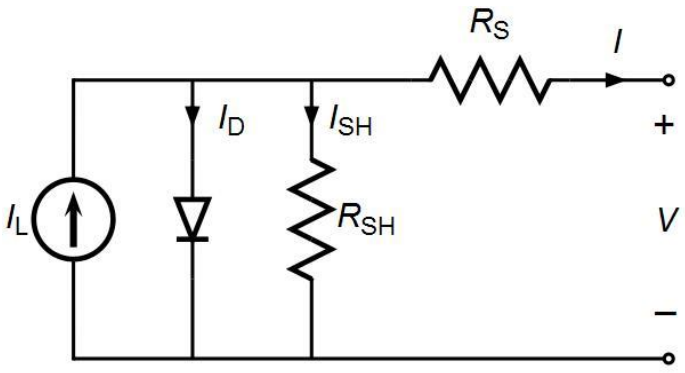

Figure 2-5 Equivalent circuit model of a dye-sensitized solar cell

R_S is usually determined by the inverse of the slope of the J-V curve when current density (*J*) is 0. It can be affected by the transparent conducting oxide layer, the morphology of the semiconductor, and the redox electrolyte. (See **Fig. 2-6**) R_{SH} is determined by the inverse of the slope of the J-V curve when voltage (*V*) is 0. It is usually affected by recombination at the surface of the transparent conducting layer and the redox electrolyte. As the series resistance increases, the J-V curve will change from the blue line in **Fig. 2-6(a)** to the red line in **Fig. 2-6(b)**. From this information, some possibilities can be predicted. The first might be the high sheet resistance of transparent

conducting oxide. The second might be that the electrons have poor transport ability in the n-type semiconductor. The third would be the poor conductivity of the redox electrolyte. When the shunt resistance decreases, the J-V curve will change from the blue line in **Fig. 2-7(a)** to the red line in **Fig. 2-7(b)**. As this happens, a partial short at the interface of the electrolyte and the transparent conducting oxide layer can be predicted. This also indicates that the nanostructured semiconductor layer is not uniform, so that this layer cannot fully isolate the conducting layer and the redox electrolyte.

Ideal I-V characteristics:

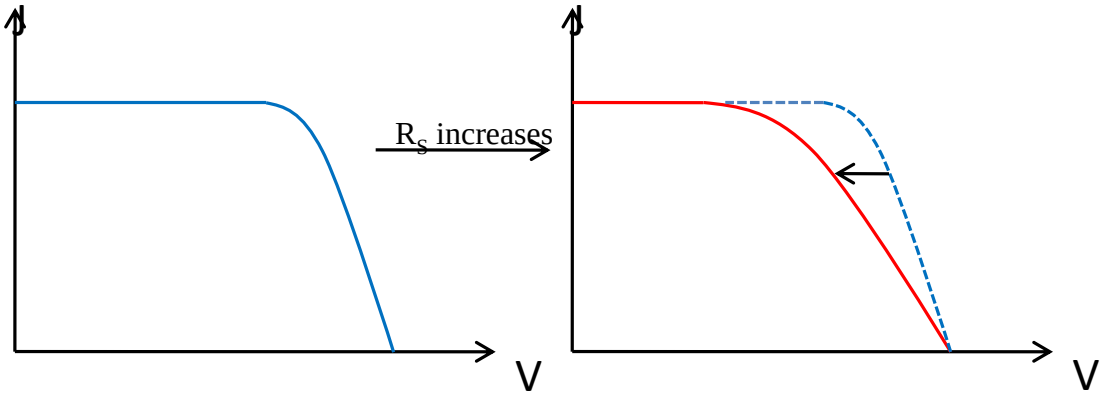

Figure 2-6 When R_S increases, the ideal J-V curve (blue line) will change to red curve

Ideal I-V characteristics:

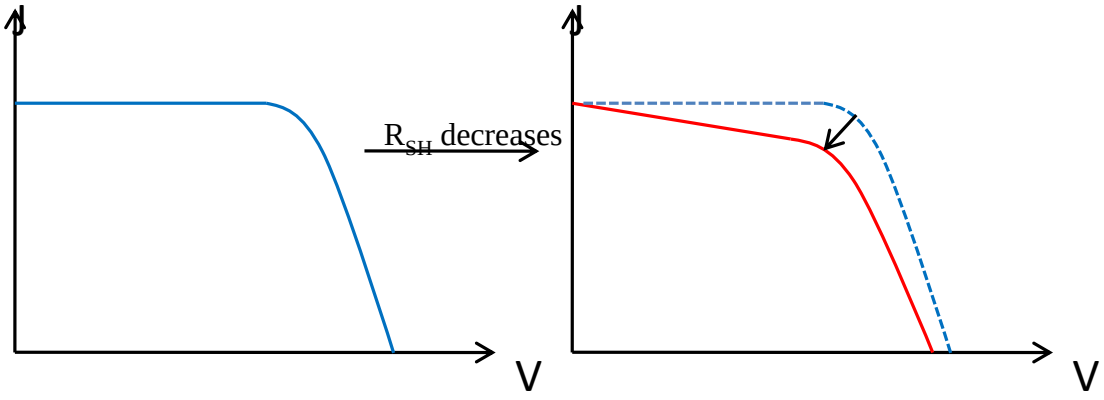

Figure 2-7 When R_{SH} decreases, the ideal J-V curve (blue line) will change to red curve

d. Power conversion efficiency(η):

Power conversion efficiency is defined as follows:

$$\eta = \frac{P_m}{P_0} = \frac{FF \times I_{sc} \times V_{oc}}{P_0} \qquad (2.2)$$

, where P_0 is the incident optical power.

e. Incident photon to current efficiency (IPCE):

Incident photon to current efficiency is defined as the following:

$$IPCE(\lambda) = \frac{\#\ of\ generated\ carriers}{\#\ of\ incident\ photons} \times 100\%$$

$$= \eta_{abs} \times \psi_{inj} \times \eta_{coll} \qquad (2.3)$$

where η_{abs} is absorption efficiency or light-harvesting efficiency,

ψ_{inj} is charge-injection efficiency,

η_{coll} is carrier-collection efficiency,

and λ is the wavelength of incident light.

η_{abs} is usually determined by the ability of dyes to catch the photons. The surface area of the nanostructured photoelectrode for dye attachment. ψ_{inj} depends on how dyes couple with the semiconductor (TiO_2), the energy position of dyes' LUMO level, and the conduction band of the semiconductor. η_{coll} depends on the charge transport ability in the nanostructure semiconductor and recombination at the surface of the photoelectrode. By integrating $\mathrm{IPCE}(\lambda) \cdot \mathrm{I_{SUN}}(\lambda)$ verse wavelength (λ), the overall short -circuit current density (I_{sc}) can be derived.

$$I_{sc} = \int_0^{\infty} IPCE(\lambda) \cdot I_{SUN}(\lambda)\ d\lambda \qquad (2.4)$$

where $\mathrm{I_{SUN}}(\lambda)$ is the spectral intensity of solar emissions.

2.3 Motivation

A dye-sensitized solar cell (DSSC) is one of the most promising next-generation solar cells because (1) it offers a relatively high photo-to-electric energy conversion efficiency 11.2 percent; (2) it has a lower manufacturing cost than that of a silicon solar cell; (3) it can be fabricated on flexible substrate; and (4) it is expected that it can meet

the stability requirement (i.e., outdoor operation for at least twenty years) [2.11-2.12].

To further enhance the competitiveness of DSSC technology and expedite the commercialization process, a higher conversion efficiency (e.g. ~15 percent, approximating the efficiency of a commercial silicon solar cell) is expected. Many research groups have developed different methods to achieve this goal, and those approaches may be classified into two categories.

One category is to develop new dyes that can offer higher efficiency. Unfortunately, it is a challenging job to develop high-efficiency new dyes. For example, although there have been significant investigations in this field, the highest efficiency DSSC achieved by the *cis*-diisothiocyanato-bis(2,2'-bipyridyl-4,4'-dicarboxylato) ruthenium(II) bis(tetrabutylammonium) dye (N-719) (see **Fig. 2-8**) was developed over a decade ago.

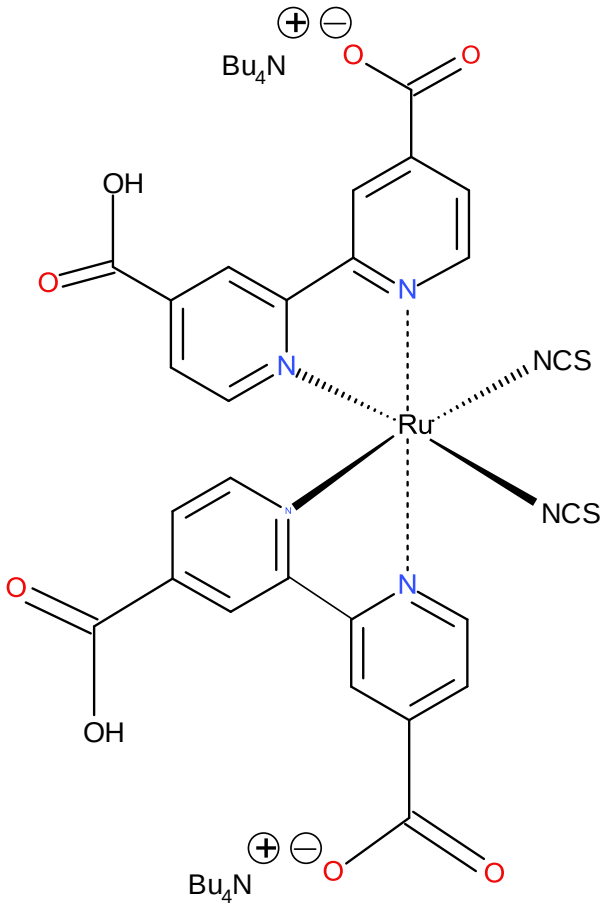

(a)

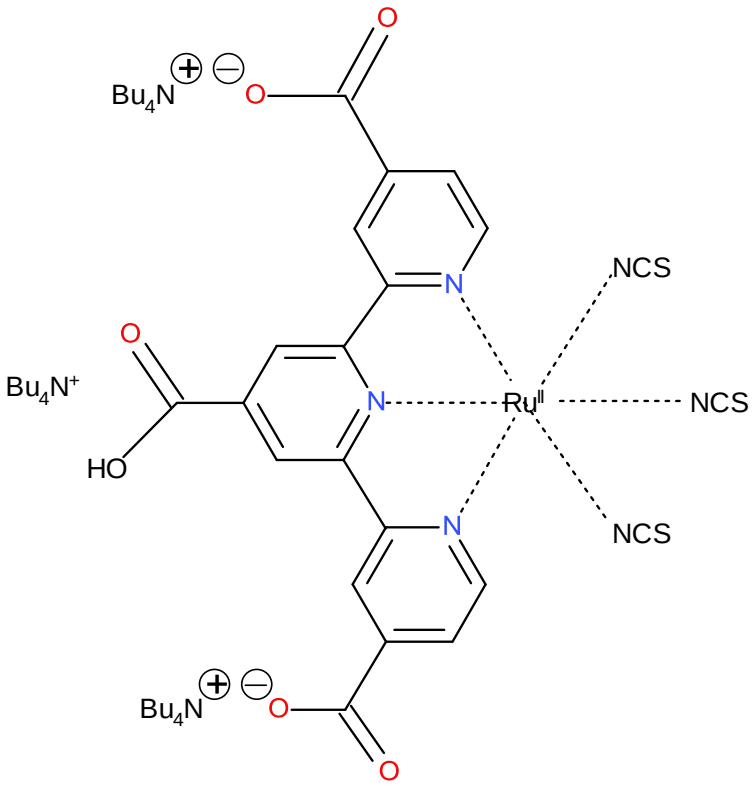

(b)

Figure 2-8 (a) molecule structure of N719 (b) molecule structure of N749 (black dye)

The other approach is to improve the efficiency by developing new semiconductor bandgap materials and structures with existing dyes. This can be a very promising approach. For example, according to the theoretical calculation of Ref. 4, the efficiency of triisothiocyanato-(2,2':6',6"-terpyridyl-4,4',4"-tricarboxylato) ruthenium(II) tris(tetrabutyl-ammonium) dye (N-749 or black dye) could be over 15 percent because

it has an absorption onset at ~ 900 nm, as illustrated in **Fig. 2-9.**

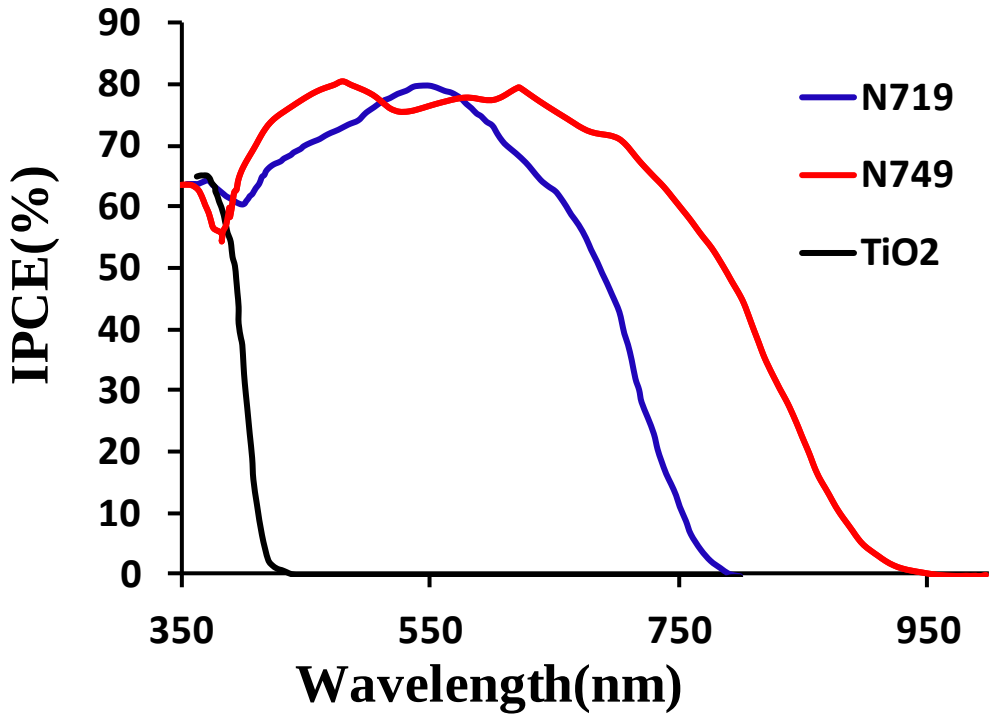

Figure 2-9 A schematic illustration of absorption curves of N719, black dye (N-749), and TiO_2

However, the maximum efficiency of DSSC with black dye is only around 11.1 percent [2.2], which is substantially lower than the theoretical value of Ref. 2.4. This is mainly due to the recombination between photo-generated electrons and oxidized dye molecules and/or electron-accepting species such as electrolyte during the charge transport process. Thus, in the conventional DSSC structure [e.g. with titanium dioxide

(TiO_2) nanoparticles], there is a fundamental tradeoff between the light-harvesting efficiency, $\eta_{LHE}(\lambda)$, and the recombination rate. To increase the light-harvesting efficiency, particularly at the longer weak absorption wavelengths (i.e., 700-900 nm), a thicker photoelectrode (i.e., higher surface area for dyes) to increase $\eta_{LHE}(\lambda)$ for DSSC is needed. To achieve high conversion efficiency, a high $\eta_{LHE}(\lambda)$ is needed over a broad spectral range (e.g. $\eta_{LHE}(\lambda) > 90\%$ over a 400 nm-900 nm spectral range). Since $\eta_{LHE}(\lambda)$ is related to the effective thickness of the film, to have a numerical idea of the required thickness, we conducted theoretical analyses for the most popular dyes (i.e., N-719 and N-749). In the simulation, a typical dye concentration value (i.e., $7.73\ x10^{-5} mol \cdot cm^{-3}$) was assumed. This value is close to the density of dyes which are coated on traditional TiO2 nanoparticle (P25)-based photoelectrodes (see **Fig. 2-11**). **Figs. 2-10(a)** and **2-10(b)** depict the molar extinction coefficients as a function of wavelength for N-719 and N-749 dyes, respectively. Based on these data, **Figs. 2-10(c)** and **2-10(d)** show the required effective thickness as a function of wavelength for N-719 and N-749 dyes, respectively. It can be seen that an effective thickness of around twenty microns is needed at shorter visible wavelengths (e.g. < 600 nm). However, a much larger effective thickness (~ 100 microns) is required at longer

(near-IR) wavelengths due to the lower molar extinction coefficients at those longer wavelengths. Even considering the enhancing effect on the effective thickness due to light scattering by the TiO_2 nanostructures, an actual thickness on the order of tens of microns is needed.

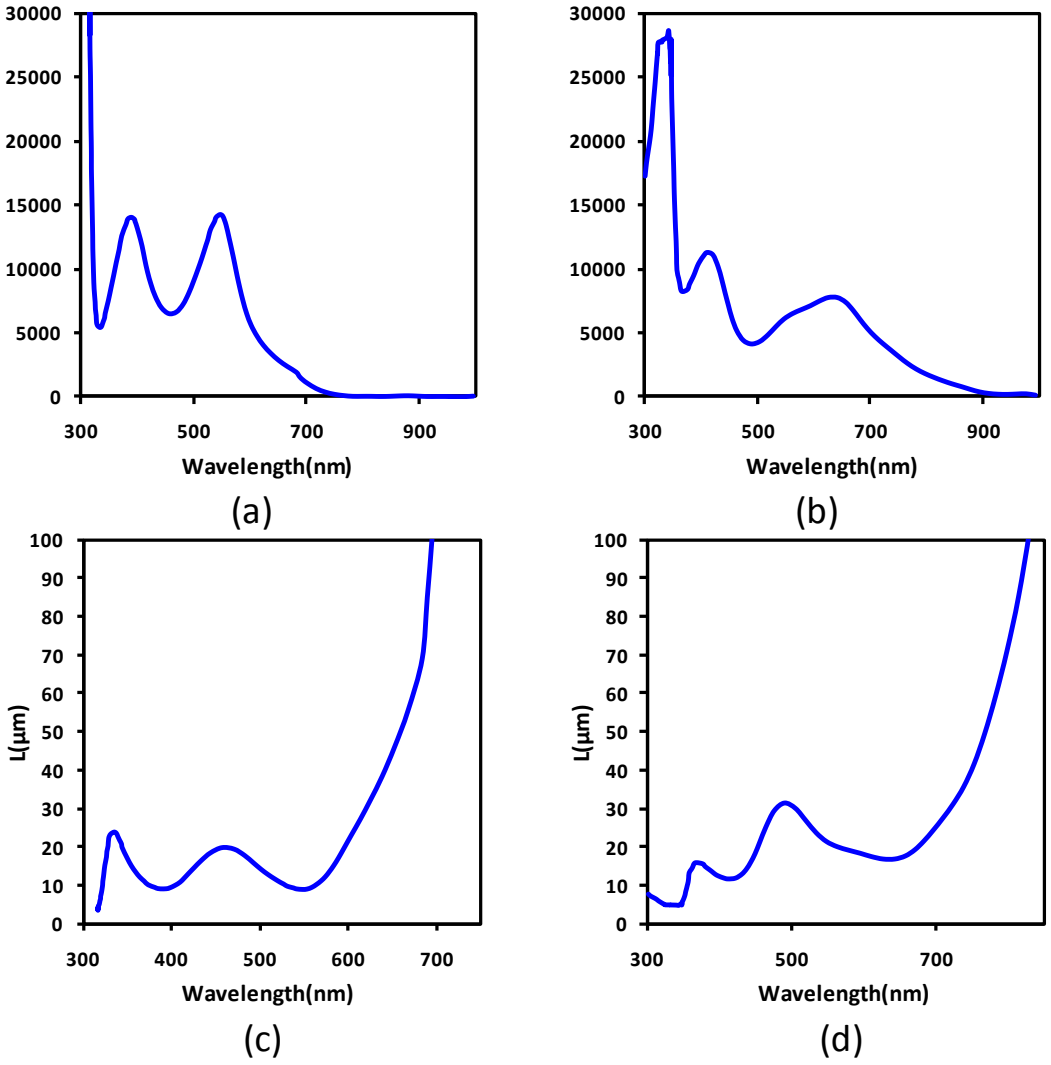

Figure 2-10 (a) A schematic illustration of molar extinction coefficient of N-719 as a function of wavelength. (b) A schematic illustration of molar extinction coefficient of N-749 as a function of wavelength. (c) A schematic illustration of required effective

thickness for achieving a 90% light-harvesting efficiency as a function of wavelength for N-719 dye. (d) A schematic illustration of required effective thickness for achieving a 90% light-harvesting efficiency as a function wavelength for N-749 dye.

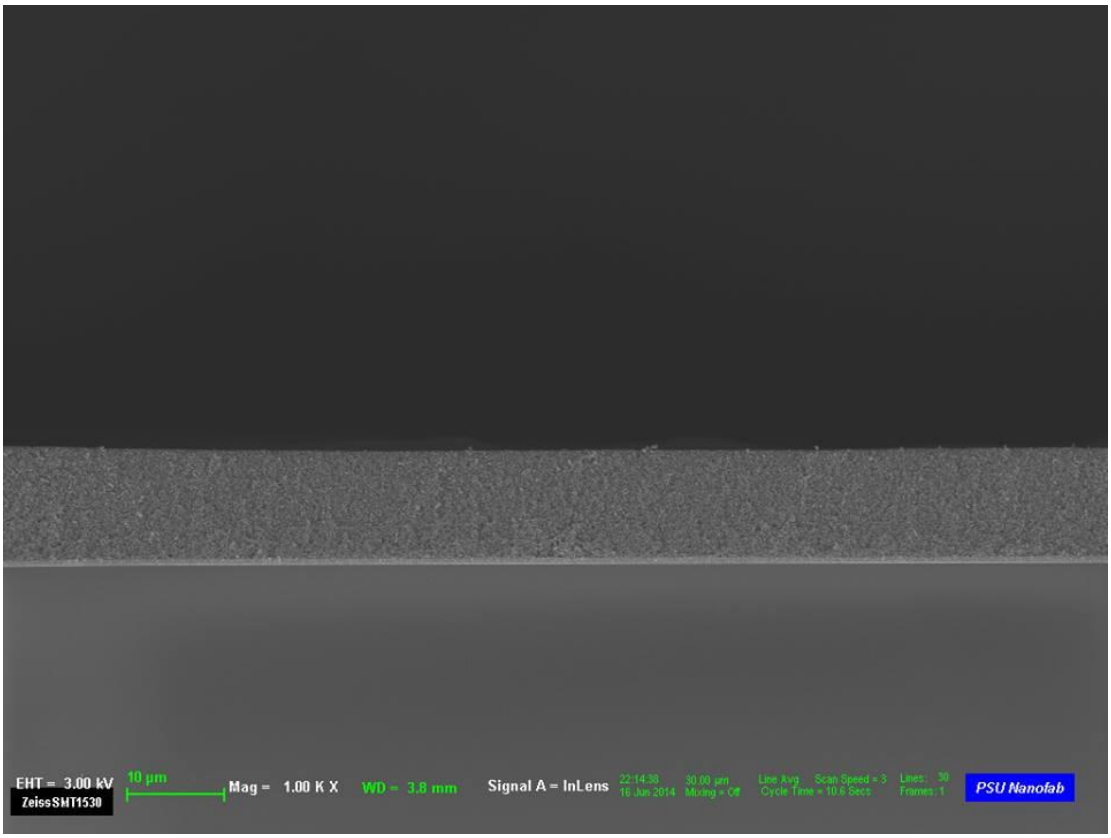

Figure 2-11 A traditional TiO2 nanoparticle (P25)-based photoelectrode fabricated with blade-paste method. The density of the dyes distributed on this photoelectrode is around $7.73\ x10^{-5} mol \cdot cm^{-3}$.

Unfortunately, the longer charge transport distance increases the recombination rate. It is extremely challenging to achieve a high electron-collection efficiency, η_{CCE}, for such a long effective thickness (i.e., ~ 100 microns) due to the limited electron diffusion length. To realize the collection of a charge carrier, the electron diffusion

length, L_{EDL}, must be greater than the effective thickness of the film, d_{eff}, as given by

$$L_{EDL} > d_{eff.} \qquad (2.5)$$

Since the typical value of L_{EDL} is only within the range of 7 - 30 microns [2.8-2.10] for the conventional TiO_2-based DSSC such as TiO_2 nanoparticles, due to charge recombination through the reduction of the oxidized dye or that of the oxidized species (I_3^-) in the electrolyte at the surface of a nanostructured semiconductor, as illustrated in **Fig. 2-12**, it is almost impossible to harvest the solar spectrum within the 700-900 nm spectral regime, which represents a waste of solar energy of over 15 percent.

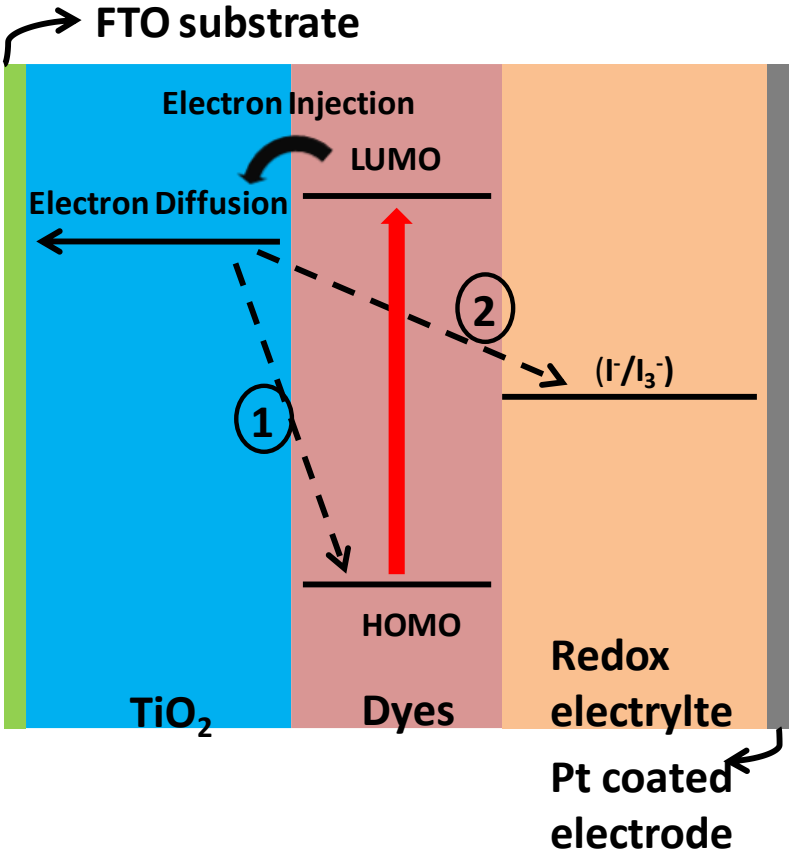

Figure 2-12 A conceptual illustration of two methods of charge recombination: (1) reduction of the oxidized dye and (2) reduction of the oxidized species in the electrolyte.

To overcome this fundamental tradeoff between the light-harvesting efficiency and the recombination rate, people have recently paid more attention to one-dimensional (1-D) structured thin films because this structure can provide a direct diffusion pathway for charges and a high surface area for application of dye-sensitized solar cells [2.9-2.10], [2.13-2.14]. Longer length and smaller diameter are usually

pursued to increase the surface area of the 1-D structure, which is conventionally identified as the key factor to increase the performance of the dye-sensitized solar cells. However, during the process of generated electron transport, the possibility of charge recombination by reduction of the oxidized dye or reduction of the oxidized species (I_3^-) at the surface of a 1-D structured semiconductor will increase with the decrease of the diameter of such 1-D structures [2.15]. Soudi's research has shown that the probability of charge recombination during the charge transport process will decrease with the diameter of the 1-D semiconductor in which charges transport. In other words, charge diffusion length in a 1-D structured semiconductor with larger diameter will be greater than that in a 1-D structured semiconductor with smaller diameter [2.10]. That is to say that pursuing infinitely smaller diameters of 1-D structures is not promising for the increase of power conversion efficiency in 1-D structure-based solar cells. Therefore, even 1-D structures can provide direct carrier transport pathways and high surface areas for dye-sensitized solar cells; the generated electrons still have a good possibility recombining with oxidized dyes or redox ions during the carrier transport process.

2.4 Methods

Our interest is to develop TiO_2 nanostructured materials that maintain a large surface area and provide a pathway through which electrons can be transported faster than those reported in 1-D nanostructured thin films and nanoparticle-composited thin films. In Chapter Three, three-dimensional TiO_2 nanoforests will be proposed **t**o overcome the drawbacks of reported 1-D TiO_2 nanostructures (i.e., crystallization and charge diffusion properties). Our group proposed three-dimensional TiO_2 structures (nanoforests) which can provide large surface areas to enhance light-harvesting efficiency and result in better electron diffusion ability. In Chapter Four, a synthesis of single-crystal anatase nanowires on transparent conducting oxide (TCO) substrates will be proposed. According to previous research, electrons have better diffusion properties in anatase crystal than in rutile crystal. However, synthesis of single-crystal nanowires on TCO substrates is more difficult than in free space. A novel method to synthesize single-crystal nanowires on transparent conducting oxide substrate (i.e., FTO glass) will be described.

2.5 References

2.1. Brain O'Regan & Michael Grätzel, "A low-cost, high-efficiency solar cell based on dye-sensitized colloidal TiO_2 films," *Nature*, vol. 353, p. 737, 1991.

2.2. Y. Chiba, A. Islam, Y. Watanabe, R. Komiya, N. Koide, and L. Han, "Dye-Sensitized Solar Cells with Conversion Efficiency of 11.1%," *Jpn. J. Appl. Phys.*, vol. 45, no. No. 25, pp. L638–L640, Jun. 2006.

2.3. M. A. Green, K. Emery, Y. Hishikawa, W. Warta, and E. D. Dunlop, "Solar cell ef fi ciency tables (version 39)," no. version 39, pp. 12–20, 2012.

2.4. H. J. Snaith, "Estimating the Maximum Attainable Efficiency in Dye-Sensitized Solar Cells," *Adv. Funct. Mater.*, vol. 20, no. 1, pp. 13–19, Jan. 2010.

2.5. H. Bürckstümmer, N. M. Kronenberg, K. Meerholz, and F. Würthner, "Near-infrared absorbing merocyanine dyes for bulk heterojunction solar cells.," *Org. Lett.*, vol. 12, no. 16, pp. 3666–9, Aug. 2010.

2.6. J. I. Basham, G. K. Mor, and C. A. Grimes, "Fo¨rster Resonance Energy Transfer in Dye-Sensitized Solar Cells," *ACS Nano*, vol. 4, no. 3, pp. 1253–1258, 2010.

2.7. P. Joshi, M. Siddiki, J. Li, D. Galipeau, Q. Qiao, H. Hall, E. Saint, J. Street, and R. City, “Pbs quantum dots embedded ti0 2 nanofibers for dye-sensitized solar cells,” *IEEE*, pp. 584–587, 2009.

2.8. S. Kolemen, Y. Cakmak, S. Erten-Ela, Y. Altay, J. Brendel, M. Thelakkat, and E. U. Akkaya, “Solid-state dye-sensitized solar cells using red and near-IR absorbing Bodipy sensitizers.,” *Org. Lett.*, vol. 12, no. 17, pp. 3812–5, Sep. 2010.

2.9. M. Law, L. E. Greene, J. C. Johnson, R. Saykally, and P. Yang, “Nanowire dye-sensitized solar cells.,” *Nat. Mater.*, vol. 4, no. 6, pp. 455–9, Jun. 2005.

2.10. O. K. Varghese, M. Paulose, and C. a Grimes, “Long vertically aligned titania nanotubes on transparent conducting oxide for highly efficient solar cells.,” *Nat. Nanotechnol.*, vol. 4, no. 9, pp. 592–7, Sep. 2009.

2.11. M. Grätzel, “Solar energy conversion by dye-sensitized photovoltaic cells.,” *Inorg. Chem.*, vol. 44, no. 20, pp. 6841–51, Oct. 2005.

2.12. M. Grätzel, “Recent advances in sensitized mesoscopic solar cells.,” *Acc. Chem. Res.*, vol. 42, no. 11, pp. 1788–98, Nov. 2009.

2.13. B. Liu and E. S. Aydil, “Growth of oriented single-crystalline rutile TiO(2) nanorods on transparent conducting substrates for dye-sensitized solar cells.,” *J. Am. Chem. Soc.*, vol. 131, no. 11, pp. 3985–90, Mar. 2009.

2.14. X. Feng, K. Shankar, O. K. Varghese, M. Paulose, T. J. Latempa, and C. a Grimes, “Vertically aligned single crystal TiO_2 nanowire arrays grown directly on transparent conducting oxide coated glass: synthesis details and applications.,” *Nano Lett.*, vol. 8, no. 11, pp. 3781–6, Nov. 2008.

2.15. A. Soudi, P. Dhakal, and Y. Gu, “Diameter dependence of the minority carrier diffusion length in individual ZnO nanowires,” *Appl. Phys. Lett.*, vol. 96, no. 25, p. 253115, 2010.

2.16. C. Pérez León, L. Kador, B. Peng, and M. Thelakkat, “Characterization of the adsorption of Ru-bpy dyes on mesoporous TiO2 films with UV-Vis, Raman, and FTIR spectroscopies.,” *J. Phys. Chem. B*, vol. 110, no. 17, pp. 8723–30, May 2006.

2.17. K. S. Finnie, J. R. Bartlett, and J. L. Woolfrey, “Vibrational Spectroscopic Study of the Coordination of Complexes to the Surface of Nanocrystalline Titania,” *Langmuir*, vol. 14, pp. 2744–2749, 1998.

2.18. K.-J. Hwang, S.-J. Yoo, S.-S. Kim, J.-M. Kim, W.-G. Shim, S.-I. Kim, and J.-W. Lee, “Photovoltaic Performance of Nanoporous TiO₂ Replicas Synthesized from Mesoporous Materials for Dye-Sensitized Solar Cells,” *J. Nanosci. Nanotechnol.*, vol. 8, no. 10, pp. 4976–4981, Oct. 2008.

Chapter 3
Multi-step Hydrothermally Synthesized TiO_2 Nanoforests

3.1 Introduction:

A dye-sensitized solar cell (DSSC) is one of the most promising next-generation solar cells because (1) it offers a relatively high photo-to-electric energy conversion efficiency 11.2 percent; (2) it has a lower manufacturing cost than that of a silicon solar cell; (3) it can be fabricated on flexible substrate; and (4) it is expected that it can meet the stability requirement (i.e., outdoor operation for at least twenty years) [3.1-3.4]. To further enhance the competitiveness of DSSC technology and expedite the commercialization process, a higher conversion efficiency (e.g. ~15 percent, which is closer to the efficiency of a commercial silicon solar cell) is desperately needed. Titanium dioxide (TiO_2) is widely used for DSSCs because it has a wide band gap and a superior charge diffusion coefficient. In recent years, one-dimensional (1-D) nanostructured TiO_2 thin films (including 1-D nanorods and 1-D nanotubes) were proposed and investigated for the DSSC application [3.5-3.12] because they can

provide a much longer electron diffusion length than that of the conventional TiO_2 nanoparticle-based structure. However, there is a fundamental tradeoff between the size of the dye absorption area and electron diffusion length for the 1-D nanostructured TiO_2 thin film. For example, the larger diameter 1-D nanorod has a lower recombination rate during the charge transport process, but it also results in a smaller surface area [3.13].

As discussed in the previous chapter, there is a tradeoff between the light-harvesting efficiency and the electron-collection efficiency when developing nanostructures for the application of dye-sensitized solar cells. To overcome this issue, a new type of DSSC using a ZnO nanoforest as the wide-bandgap oxide semiconductor was recently reported [3.14]. In this structure, the trunks of the nanoforest served as the charge conduction pathways, increasing the electron diffusion length and reducing the charge recombination rate; meanwhile, the branches of the nanoforest offered a large light absorption surface area, ensuring good light-harvesting efficiency. However, due to the poor electron injection efficiency from excited dyes to ZnO, caused by the dissolution of ZnO and precipitation of day-Zn^{2+} complex [3.15], the conversion efficiency reported in Ref. 14 was still low (~ 2.63 percent even with a backbone trunk length of 13 microns). Compared with ZnO, TiO_2 is a relatively stable high bandgap

semiconductor material for DSSCs because of its higher charge injection efficiency.

In this chapter, by using a unique multi-step hydrothermal growing process (to be described in detail in next section), a TiO_2 nanoforest was successfully grown. The TiO_2 nanoforest is composed of an array of nanotrees, as illustrated. Each nanotree consists of a trunk (also called a nanorod) that has a diameter on the order of hundreds of nanometers, branches (also called nanowires) that has a diameter on the order of tens of nanometers, and dyes attached on the branches, as illustrated in **Fig. 3-1**. The large diameter of the trunk and its continuous one-dimensional structure (unlike a nanoparticle network that has many contact interfaces, reducing the electron diffusion length) results in a good carrier transportation. In other words, the trunk serves as an electron carrier pathway, which ensures a long electron diffusion length that results in high electron-collection efficiency. On the other hand, the large surface area of the branches produces a high light-harvesting efficiency.

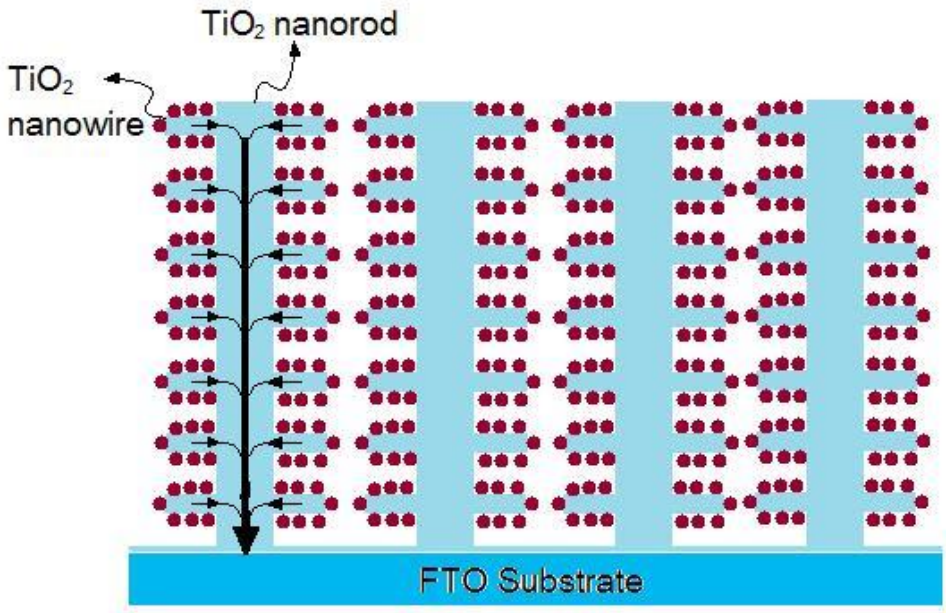

Figure 3-1 The electron diffusion length in a TiO_2 nanorod is longer than that in a TiO_2 nanowire. Charge recombination happens less frequently during electron transport in a TiO_2 nanorod than in a TiO_2 nanowire.

In short, the TiO_2 nanoforest provides all the required characteristics for achieving a high $IPCE(\lambda)$ over a broad spectral range (e.g. >80 percent over the 400 nm-900 nm for the black dye N-749), including a high light-harvesting efficiency (offered by the large surface area of the branches), (2) a high electron-collection efficiency due to the existence of the electron carrier pathway (provided by the trunks), and (3) a high charge-injection efficiency because of the excellent contact between the TiO_2 material and the dye. Thus, according to the theoretical prediction of Ref. 5, a higher

conversion (over 15 percent) is achievable.

3.2 Experimental methods and procedures

3.2.1 Hydrothermal/solvothermal synthesis

Hydrothermal/solvothermal synthesis is a method to synthesize crystal nanostructures in the environment with high-temperature saturated solution and high-pressure vapor. The crystallization process is conducted in autoclaves. An autoclave is usually composed of a Teflon reactor and a metal bomb (see **Fig. 3-2**). To conduct a hydrothermal process, a substrate containing solution and precursor is placed in the autoclave. When the autoclave is heated, supersaturation will occur, causing the crystal metal-oxide seed nucleate on the substrate and the metal oxide to grow along the direction of the crystal. The morphology and size of the metal oxide can usually be controlled by changing the substrates, precursors, solvents, temperature, reaction time, concentration of the solution, and pH value of the solution.

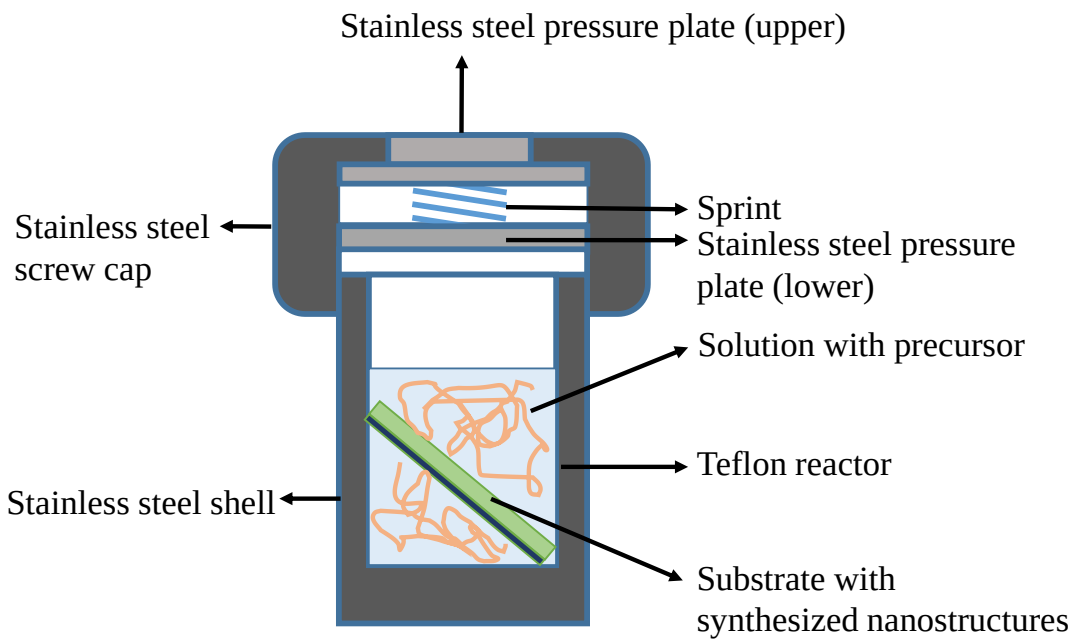

Figure 3-2 A schematic of a metal bomb and a Teflon reactor set up to perform a hydrothermal synthesis

3.2.2 Synthesis of a TiO_2 nanoforest

A unique multi-step hydrothermal process was used to synthesize a TiO_2 nanoforest, as illustrated in **Fig. 3-3**. First, fluorine-doped tin oxide (FTO) glass substrates (TEC8/TEC15) were well cleaned by ultrasonication in ethanol, isopropanol, and acetone for ten minutes each. Then a two-step hydrothermal process was used to synthesize a TiO_2 nanoforest, as described below:

3.2.2.1 Growth of TiO_2 nanorods (trunks)

The first step was to synthesize a TiO_2 nanorod (i.e., trunk) on the cleaned FTO substrate. FTO glass substrates were put in a Teflon reactor which contained a mixture of a solution of DI water (30 mL), HCl aqueous solution (30 mL with a 37 percent concentration), and titanium butoxide (0.5 mL). The reactor was sealed in the metal bomb and baked at a temperature of 150℃ for six to twenty hours.

3.2.2.2 Growth of TiO_2 nanowires (branches)

The second step was to synthesize TiO_2 nanowires (i.e., branches) on the previously synthesized TiO_2 nanorods with following procedures. First, after rinsing the samples with deionized (DI) water and ethanol for several times and drying with gentle nitrogen flow, the TiO_2 nanorod samples were transferred to another Teflon reactor that contained 10 mL toluene, 0.25 mL to 2.0 mL titanium butoxide, 1 mL HCl aqueous solution (37 percent), and 1 mL $TiCl_4$ solution (1 M in toluene). Second, the reactor was sealed in a metal bomb again and baked at a temperature of 180℃ for several hours. Finally the sample was removed from the reactor, rinsed with DI water and ethanol several times, and annealed at a temperature of 450℃ for one hour.

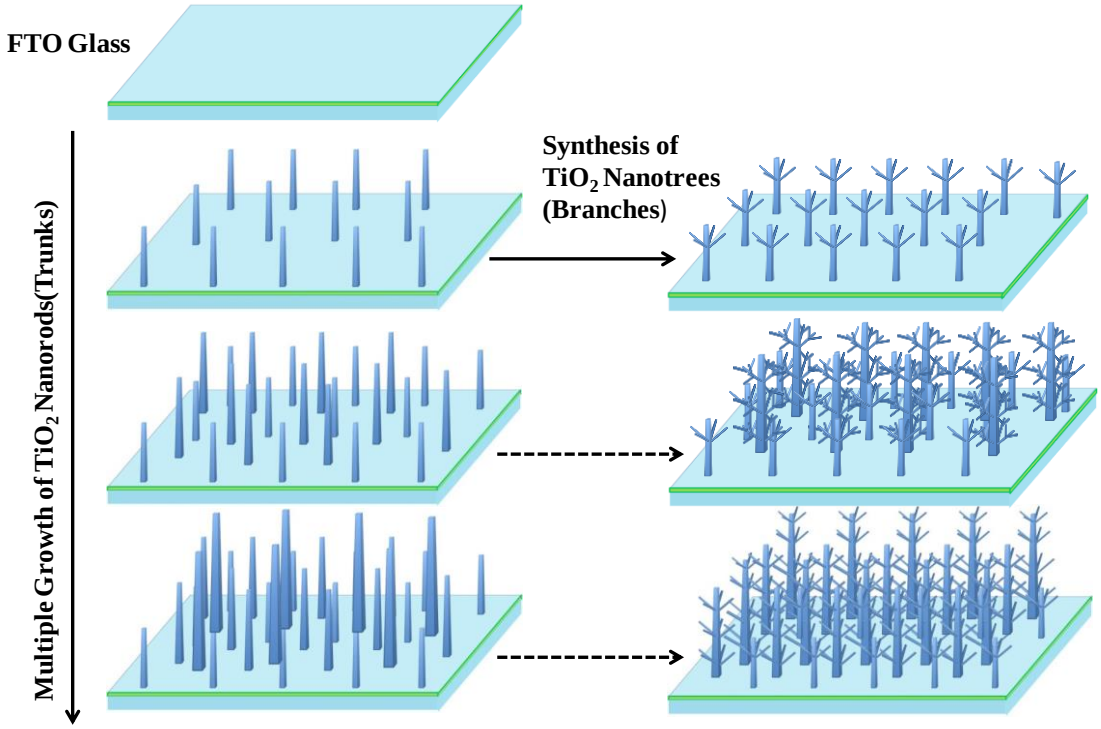

Figure 3-3 Nanotree synthesis procedure: TiO_2 nanorods are synthesized on FTO glass substrate by a multi-step hydrothermal process. TiO_2 nanowires are then synthesized on TiO_2 nanorods using the solvothermal method.

3.2.3 Fabrication and testing of TiO_2-nanoforest-based DSSCs

3.2.3.1 Fabrication of DSSCs based on TiO_2 nanoforests

The DSSC was fabricated after synthesizing a TiO_2 nanoforest using the procedures described below. First, TiO_2 nanoforest samples were immersed in 0.3mM N-719 dye (made by Solaronix Inc., Switzerland) solution for twenty-four hours. Second, the Redox electrolyte was synthesized by mixing a commercial electrolyte (MPN-100, Solaronix Inc., Switzerland) with acetonitrille that contained 0.1 M LiI at a ratio of 1:2.

Third, a 25μm hot-melt spacer SX-1170-25PF (Solaronix Inc., Switzerland) was loaded between nanoforest sample and counter electrode of platinum (Pt) coated FTO glass. Finally, DSSC was fabricated by filling Redox electrolyte into the sandwiched structure.

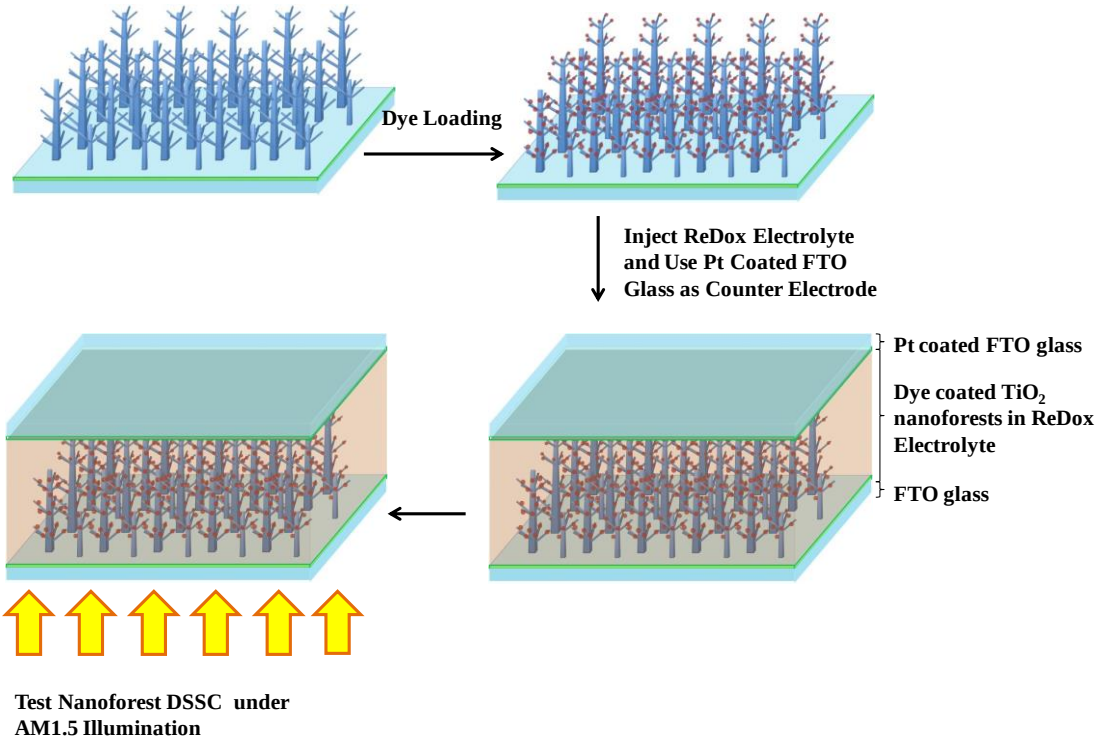

Figure 3-4 The synthesized nanotrees are sensitized with dyes. Redox electrolyte is filled in the Pt coated counter electrode and the sensitized nanotrees. The DSSC is tested under AM1.5 illumination.

3.2.3.2 Experiment setup of I-V measurement and test of DSSCs

The performance of TiO_2 nanoforest based DSSC samples was quantitatively tested with a standard AM1.5 solar simulator made by Newport Corporation. The experiment setup of I-V measurement is shown in **Fig. 3-5**. This setup includes (1) a solar simulator,

(2) a power supply of solar simulator, (3) a computer with LabVIEW based I-V characterization software, (4) a multimeter, and (5) a DC power supply. The solar simulator can generate AM 1.5 incident light, which is a simulated sun light. To gain the I-V curve of the DSSCs under AM 1.5 illumination, a DC voltage is fed to the positive electrode of a DSSC. At the same time the positive and negative electrodes are connected to a multimeter. A computer with LabVIEW based I-V characterization software is connected to the multimeter to record the data of voltages and currents generated from the tested device.

Figure 3-5 Setup of solar simulator

3.3 Results and discussion

By using the procedures as described in Section 3.2.1, TiO_2 nanorods with a length around 2μm and a diameter of several hundred nanometers were synthesized in one single round hydrothermal process. The density of nanorods synthesized on FTO substrate was controlled by the concentration of titanium precursor. Furthermore, to achieve a long nanorod without making them contact each other, a multi-step growing

process was employed. As reported in Ref. 3-11, the maximum length of TiO_2 nanorod was only about 2.8 microns if only one growing cycle was used because the growing solution reached the chemical equilibrium state after certain time (e.g. twenty hours). In our experiment, eight growing cycles were used and the growing time for each cycle was around six hours. In each growing cycle, a fresh solution with the same composition was employed. Thus, the nanorod could continue to grow without the maximum length limitation of the conventional one-cycle growing method, since a chemical equilibrium condition was not reached during each growing cycle.

To achieve a large surface area for the nanoforest, longer nanorods and greater spacing between adjacent nanorods are needed. The length and spacing of nanorods depends on the length of baking time and the baking temperature of hydrothermal process. Longer baking time and higher baking temperatures can result in longer nanorods. However, they can also reduce the spacing between adjacent nanorods. To avoid contact of adjacent nanorods, can result in a reduced surface area, the length of the baking time for each cycle was shortened to six hours rather than twenty hours as used in Ref. 3.11. Observation of the growing process of the nanorods showed that nothing appeared on the surface of the FTO substrates when the growing time was less

than three hours. The nanorods began to grow on the FTO substrates after three hours, and the density of nanorods on the FTO substrates increased as well. To restrain the increase rate of the density of nanorods, the hydrothermal process was terminated at the end of each six-hour period. After cooling down, the samples were transferred to a fresh solution immediately for the next step of process. The advantage of this process is that existing nanorods would continue to grow for each new hydrothermal cycle, but new nanorods would only appear after three hours, which reduces the generation rate of new nanorods so that longer nanorods with larger spacing among them can be achieved.

The ambient condition for the hydrothermal process was set as 30 mL DI water + 30 mL HCl aqueous solution (37 percent concentration) + 0.5 mL titanium butoxide. The experimental result showed that there were no noticeable grown nanorods after the first and second growing cycles. However, one could start to observe grown nanorods after the third growing cycle. As an example, **Figs. 3-6(a)** and **3-6(b)** showed the scanning electron microscope (SEM) images of the top and cross-section views of the grown nanorods after the third growing cycle. One could clearly see the grown nanorods. The average length and diameter of the nanorods were around 1.3μm and

50nm, respectively.

With the increase in the number of hydrothermal process cycles, the length, diameter, and numbers of the nanorods are all increased. **Fig. 3-6(g)** and **3-6(h)** show the top and cross-section views of the TiO_2 nanorods after eight growing cycles. It can be observed that the average length and diameter of the nanorods were around 4.1μm and 300nm, respectively. These experimental results clearly demonstrated that longer nanorods could indeed be grown by employing the multi-step growing technique as described. Furthermore, since the growth occurs in both longitudinal and transversal directions (i.e., the nanorod becomes thicker after each growing cycle), in order to avoid the contact among adjacent nanorods, the separation distance for the initial growing cycle was controlled by adjusting the growing conditions (e.g. the baking temperature and time).

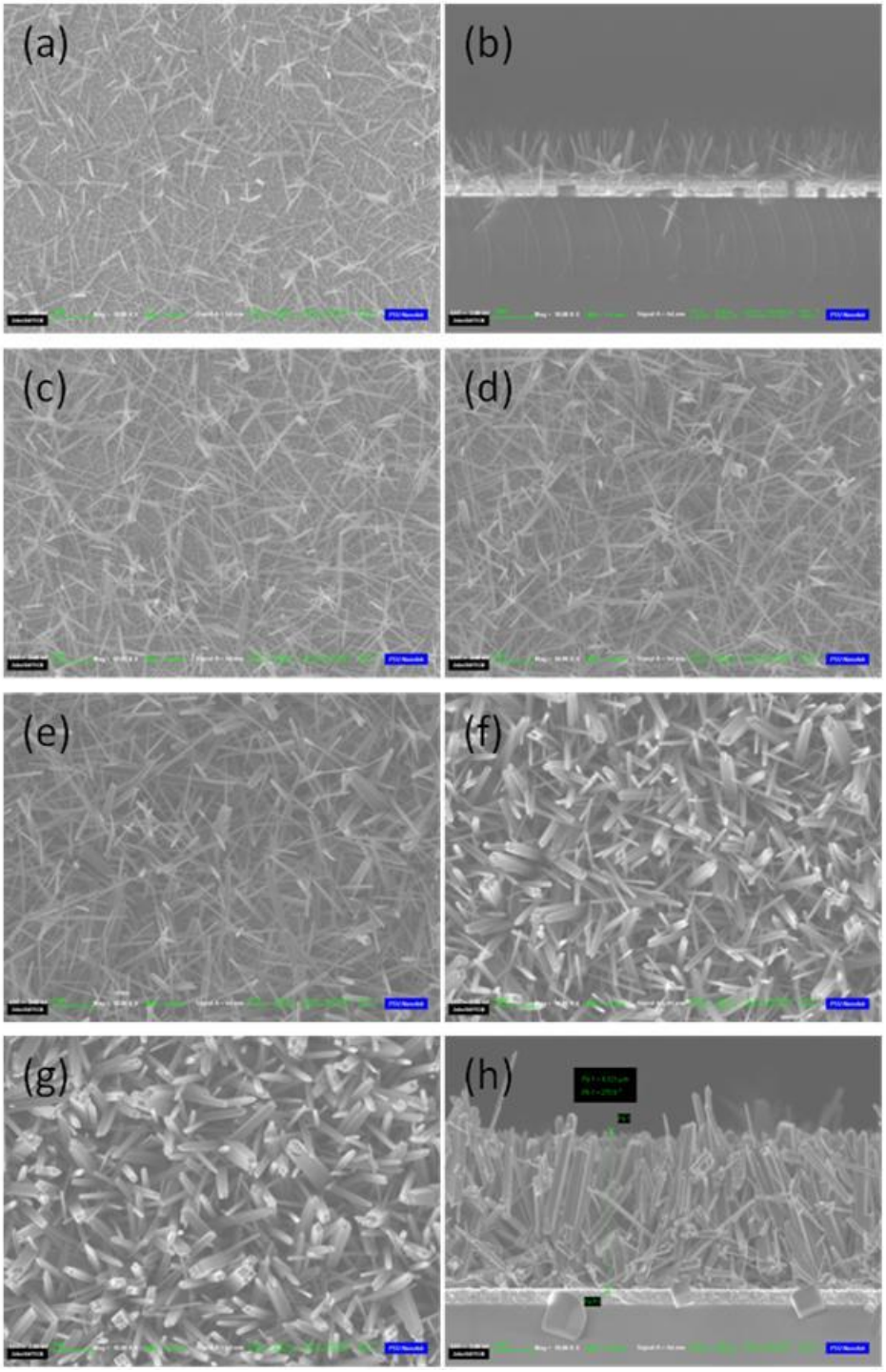

Figure 3-6 (a-b) Top and cross-section views of TiO_2 nanorods after three growing cycles, showing an average length of around 1.3 μm and a diameter of around 50 nm. (c-f) Top views of TiO_2 nanorods after four, five, six, and seven growing cycles, respectively. (g-h) Top and cross-section views of TiO_2 nanorods after eight growing

cycles showing an average length of around 4.1 μm and a diameter of around 300 nm.

For the second step of the hydrothermal process, a non-polar solvent, toluene, was adopted as the main solvent to synthesize smaller-diameter TiO_2 nanowires as branches. The nanowires were grown on the nanorod substrates synthesized during the first step of hydrothermal process. The growing rate, direction, and dimension of the nanowire depended on the concentration of the titanium precursor. The experimental results showed that nanowires had a tendency to grow in vertical directions as the concentration level of the titanium precursor increased (e.g. > 2.0 mL of titanium precursor added in 10 mL toluene). As an example, **Fig. 3-7(a)** is a conceptual drawing of the grown nanowires on nanorods under these conditions. **Figs. 3-7(b)** and **3-7(c)** showed the SEM images of the top and cross-section views of the grown nanowires on nanorods (with a length of around 1.3 μm). It clearly shows a nanoforest structure. The total height of the nanoforest is around 2.4 μm. The length of the nanowires can be over 1 μm and the average diameter of the nanowire is less than 30 nm. It is noted that although nanowires can also grow on TCO substrate, they can only grow a thin layer (< 100 nm) because further growth in the upper direction is blocked by the nanowires grown on the nanorod.

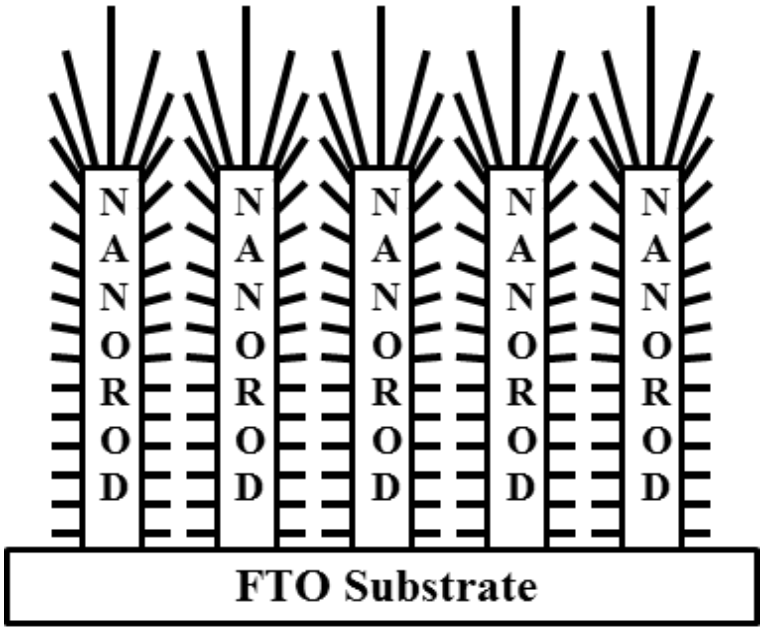
NANOROD
NANOROD
NANOROD
NANOROD
NANOROD
FTO Substrate

(a)

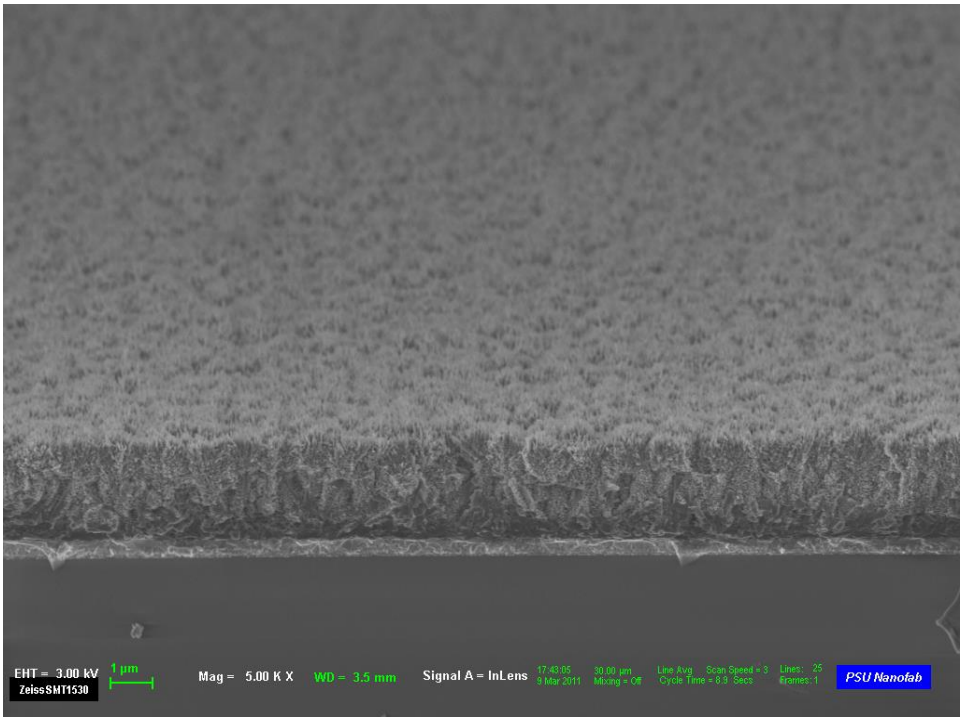
EHT = 3.00 kV
ZeissSMT1530
1 µm
Mag = 5.00 K X
WD = 3.5 mm
Signal A = InLens
PSU Nanolab

(b)

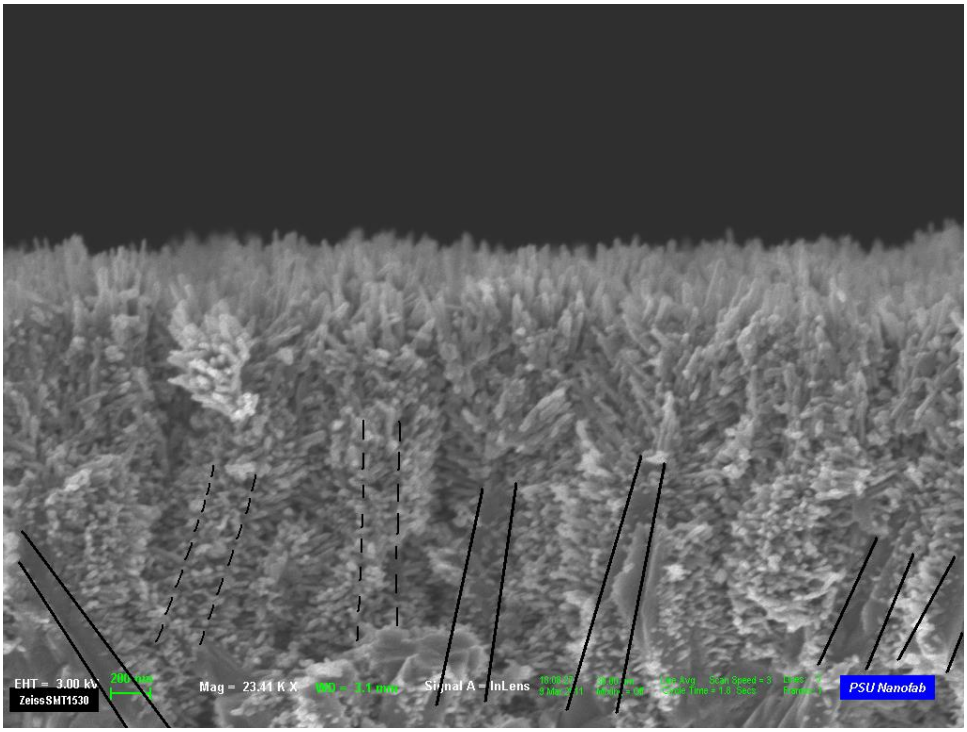

(c)

Figure 3-7 (a) A conceptual illustration of the grown nanowires on nanorod substrates. (b) An SEM image of the top view of the grown nanowires on nanorod substrates, showing a nanoforest configuration. (c) An SEM image of the cross-section view of the grown nanowires on nanorod substrates, showing a nanoforest configuration.

Finally, a set of TiO_2-nanoforest-based DSSCs with different heights of nanoforest from 1.5μm to 5.1μm were synthesized by using procedures described in Section 2.2. The performance of the DSSCs was also quantitatively tested with a standard AM1.5 solar simulator made by Newport Corporation. The important parameters of the solar cell, including the photocurrent-voltage curve, the short-circuit current density, the

open-circuit voltage, and the fill factor were measured. Based on these measured data, the conversion efficiency, η, was also calculated using the following equation:

$$\eta = \frac{J_{SC} V_{oc} FF}{I_s}, \qquad (3.1)$$

where J_{SC} denotes the short circuit photocurrent density, V_{oc} represents the open-circuit photovoltage, FF stands for the fill factor, and I_s is the intensity of the incident light.

Table 1 and **Fig. 3-8** summarize the testing results for Samples 1, 2, 3, 4, and 5, of which the thickness are 1.5, 2.0, 2.3, 3.7, and 5.1 microns, respectively. It can be clearly seen that the conversion efficiency increases as the height of the nanoforest increases due to the increased surface area. The conversion efficiency is up to 3.93 percent for a 5.1 μm-height TiO_2 nanoforest, which is much higher than that of a DSSC based on a ZnO nanoforest. For instance, the conversion efficiency of a ZnO nanoforest is only about 2.63 percent even when the thickness of the ZnO nanoforest is thirteen microns, which is substantially lower than the conversion efficiency achieved with a 5.1-micron-thick TiO_2-nanoforest-based DSSC. Thus, a TiO_2-nanoforest-based DSSC can offer a

much higher conversion efficiency than that of a ZnO-nanoforest-based DSSC when the thickness of the nanoforest is the same. This is because a TiO_2 nanoforest has a higher electron-injection efficiency than a ZnO nanoforest [3.15].

	Thickness(μm)	Efficiency (%)	J_{SC}(mA/cm^2)	V_{OC}(V)	Fill Factor
Sample1	1.5	0.04	0.28	0.504	0.30
Sample 2	2.0	0.58	1.15	0.797	0.63
Sample 3	2.3	1.25	2.57	0.774	0.63
Sample 4	3.7	2.50	4.90	0.756	0.67
Sample 5	5.1	3.93	7.30	0.787	0.68

Table 3-1 Characteristics of a TiO_2-nanoforest-based DSSC for samples 1, 2, 3, 4, and 5, respectively.

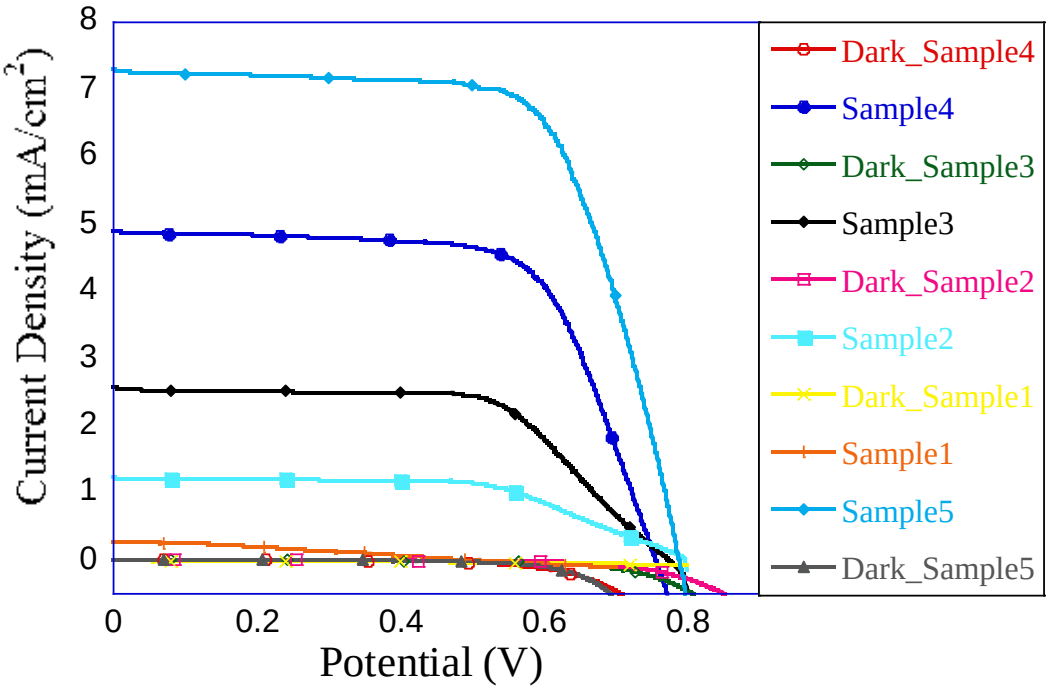

Figure 3-8 J-V characteristics of a TiO_2-nanoforest-based DSSC for Sample 1, Sample 2, Sample 3, Sample 4, and Sample 5, respectively.

It can be also noted that the reason of conversion efficiency increases with the increase of the height of the nanoforest is due to the increased surface area so that a larger amount of dyes can be attached on the surface of nanoforest, which results in a better light absorption. The conversion efficiency increases with increase in the height of nanoforest; however, it reaches a certain maximum level at certain height (e.g. twenty microns). After the majority of the light (e.g. 99.9 percent) is absorbed by dye, the further increase in height can reduce the conversion efficiency due to the reduced

transport efficiency.

3.4 Conclusion

A new type of DSSC based on a TiO_2 nanoforest was demonstrated in this research. The TiO_2 nanoforest was synthesized by using a unique multi-step hydrothermal process. There are several major advantages of TiO_2-nanoforest-based DSSCs. First, the nanoforest structure overcame a fundamental limitation of the conventional DSSC, which was the tradeoff between the light-harvesting efficiency and the electron-collection efficiency. Second, unlike a ZnO nanoforest that had a poor electron-injection efficiency, a TiO_2 nanoforest also was shown to have high electron-injection efficiency. Thus, all the required characteristics for achieving high conversion efficiency, including high light-harvesting efficiency, high electron-collection efficiency, and high electron-injection efficiency, could be achieved simultaneously, enabling the realization of low-cost high-conversion-efficiency solar cells. The experimental results confirmed that a conversion efficiency of 3.93 percent could be achieved for a TiO_2 nanoforest with a 5.1-micron trunk length, which was higher than a ZnO-nanoforest-based DSSC with a much longer trunk length (thirteen microns).

This experimental result clearly demonstrated the advantage of using TiO_2 nanoforests to replace ZnO nanoforests for DSSC applications. An even higher conversion efficiency, which will be investigated in the future, is anticipated if a longer trunk (e.g. thirteen-micron) TiO_2 nanoforest is employed, due to the increased surface area.

3.5 References

3.1. M. Grätzel, “Solar energy conversion by dye-sensitized photovoltaic cells.,” *Inorg. Chem.*, vol. 44, no. 20, pp. 6841–51, Oct. 2005.

3.2. Brain O’Regan & Michael Grätzel, “A low-cost, high-efficiency solar cell based on dye-sensitized colloidal TiO_2 films,” *Nature*, vol. 353, p. 737, 1991.

3.3. M. Grätzel, “Recent advances in sensitized mesoscopic solar cells.,” *Acc. Chem. Res.*, vol. 42, no. 11, pp. 1788–98, Nov. 2009.

3.4. Y. Chiba, A. Islam, Y. Watanabe, R. Komiya, N. Koide, and L. Han, “Dye-Sensitized Solar Cells with Conversion Efficiency of 11.1%,” *Jpn. J. Appl. Phys.*, vol. 45, no. No. 25, pp. L638–L640, Jun. 2006.

3.5. A. C. Fisher, L. M. Peter, E. A. Ponomarev, A. B. Walker, and K. G. U. Wijayantha, “Intensity Dependence of the Back Reaction and Transport of Electrons in Dye-Sensitized Nanocrystalline TiO 2 Solar Cells,” pp. 949–958, 2000.

3.6. S. Nakade, M. Matsuda, S. Kambe, Y. Saito, T. Kitamura, T. Sakata, Y. Wada, H. Mori, and S. Yanagida, “Dependence of TiO 2 Nanoparticle Preparation Methods and Annealing Temperature on the Efficiency of Dye-Sensitized Solar

Cells," pp. 10004–10010, 2002.

3.7. T. Oekermann, D. Zhang, T. Yoshida, and H. Minoura, "Electron Transport and Back Reaction in Nanocrystalline TiO 2 Films Prepared by Hydrothermal Crystallization," no. Iv, pp. 2227–2235, 2004.

3.8. G. K. Mor, K. Shankar, M. Paulose, O. K. Varghese, and C. a Grimes, "Enhanced photocleavage of water using titania nanotube arrays.," *Nano Lett.*, vol. 5, no. 1, pp. 191–5, Jan. 2005.

3.9. K. Shankar, G. K. Mor, H. E. Prakasam, S. Yoriya, M. Paulose, O. K. Varghese, and C. a Grimes, "Highly-ordered TiO 2 nanotube arrays up to 220 µm in length: use in water photoelectrolysis and dye-sensitized solar cells," *Nanotechnology*, vol. 18, no. 6, p. 065707, Feb. 2007.

3.10. O. K. Varghese, M. Paulose, and C. a Grimes, "Long vertically aligned titania nanotubes on transparent conducting oxide for highly efficient solar cells.," *Nat. Nanotechnol.*, vol. 4, no. 9, pp. 592–7, Sep. 2009.

3.11. B. Liu and E. S. Aydil, "Growth of oriented single-crystalline rutile TiO(2) nanorods on transparent conducting substrates for dye-sensitized solar cells.," *J. Am. Chem. Soc.*, vol. 131, no. 11, pp. 3985–90, Mar. 2009.

3.12. X. Feng, K. Shankar, O. K. Varghese, M. Paulose, T. J. Latempa, and C. a Grimes, “Vertically aligned single crystal TiO_2 nanowire arrays grown directly on transparent conducting oxide coated glass: synthesis details and applications.,” *Nano Lett.*, vol. 8, no. 11, pp. 3781–6, Nov. 2008.

3.13. A. Soudi, P. Dhakal, and Y. Gu, “Diameter dependence of the minority carrier diffusion length in individual ZnO nanowires,” *Appl. Phys. Lett.*, vol. 96, no. 25, p. 253115, 2010.

3.14. H. J. S. Seung Hwan Ko, Daeho Lee, Hyun Wook Kang, Koo Hyun Nam, Joon Yeob Yeo, Suk Joon Hong, Costas P. Grigoropoulos, “Nanoforest of Hydrothermally Grown Hierarchical ZnO Nanowires for a High Efficiency Dye-Sensitized Solar Cell,” *Nano Lett.*, pp. 666–671, 2011.

3.15. G. B. Marı´a Quintana, Tomas Edvinsson, Anders Hagfeldt, “Comparison of Dye-Sensitized ZnO and TiO 2 Solar Cells : Studies of Charge Transport and Carrier Lifetime,” *J. Phys. Chem. C*, pp. 1035–1041, 2007.

Chapter 4
Single-Crystal Anatase Nanowires

4.1 Introduction

In recent years, there has been an increased interest in nanostructured titanium dioxide (TiO_2) thin films, including nanorods, nanowires, and nanoflakes, because they can provide a direct transport pathway for photo-generated charge carriers, which is very important for a variety of clean-energy-related applications, including dye-sensitized solar cells (DSSCs) [4.1-4.4], photo-catalytic water splitting, [4.5-4.6] etc. Although high-aspect-ratio rutile TiO_2 nanorods and nanowires have been successfully grown on fluorine-doped tin oxide (FTO) transparent conductive substrates [4.7-4.8], anatase TiO_2 nanostructured thin films are preferred because their electron mobility properties are an order of magnitude higher than the rutile counterpart.

Unfortunately, it is more challenging to grow high-aspect-ratio anatase nanostructured thin films on transparent conductive substrates because rutile is a more stable state in nature. Anatase nanostructured TiO_2 nanorods and nanoflakes grown on

transparent conductive substrates were only reported very recently [4.9]. However, nanorod and nanoflake length is still very limited (around one micron), which limits the overall surface area of nanostructured TiO_2 thin films. The light-to-electricity conversion efficiency of the DSSC based on this type of nanostructured TiO_2 thin film is about 2.1 percent [4.9].

To grow thicker anatase nanostructured TiO_2 thin film on transparent conductive substrate, we present a new growing method in this chapter, describing the combination of dip coating and alkaline hydrothermal techniques [4.10], [4.11]. The length of grown anatase TiO_2 nanostructured thin film is close to 2.2 microns, and the light-to-electricity conversion efficiency of DSSCs based on this anatase TiO_2 nanostructured thin film reaches 5.2 percent, which represents a substantial technological advance in this area.

4.2. Synthesizing anatase TiO_2 nanowires on FTO substrate

The anatase TiO_2 nanowires were grown on FTO substrate by combining the dip coating and alkaline hydrothermal techniques.

4.2.1 Depositing a thin TiO_2 overlay layer on an FTO glass substrate by dip coating.

To achieve the goal of lowering the cost, the TiO_2 pre-film was deposited by the dip-coating method rather than by using various high-cost approaches (e.g. PVD or CVD).

First, FTO glass (TEC7) substrate was cleaned by ultrasonicating in acetone, isopropanol, and ethanol, rinsing with DI water, drying with nitrogen, and baking at 100℃ for one hour. Second, titanium butoxide ($Ti(OCH_2CH_2CH_2CH_3)_4$) (see **Fig. 4-1**), polyethylene glycol (PEG), and ethanol were mixed with a ratio of 1:1:2. The cleaned FTO substrates were dip-coated multiple times in the solution at a drawing speed of one cm/min and then calcined at 400℃ for ten minutes after each coating. After applying the last layer of coating, samples were kept in the furnace overnight to form bulk-like TiO_2 thin-film layers.

It should be noted that the bulk-like TiO_2 thin-film layers deposited by the dip-coating method may be discontinuous because titanium butoxide can be hydrolyzed due to the water vapor in the air, resulting in the formation of TiO_2 large-sized nanoparticles. This affects the quality of the deposited titanium butoxide thin film. To prevent the hydrolysis of titanium butoxide during the dip-coating process, polyethylene glycol (PEG) (see **Fig. 4-2**), a stable liquid polymer, was also added to

the mixture of titanium butoxide and ethanol because PEG can serve as a protective layer between the air and the titanium butoxide. After baking at 400℃ , PEG will evaporate and the rest of the uniform titanium butoxide thin film will be oxidized, resulting in a continuous bulk-like TiO_2 thin film, as given by

$$Ti(O-C_4H_9)_4 + 4H_2O \rightarrow Ti(OH)_4 + 4C_4H_9OH$$

$$Ti(OH)_4 + Ti(O-C_4H_9)_4 \rightarrow 2TiO_2 + 4C_4H_9OH$$

$$Ti(OH)_4 + Ti(OH)_4 \rightarrow 2TiO_2 + 4H_2O$$

It should also be noted that the FTO layer and substrate glass can be dissolved in the highly-concentrated aqueous NaOH solution during the later hydrothermal process via the following chemical reactions:

$$SnO_2 + 2NaOH \rightarrow Na_2SnO_3 + H_2O$$

$$SiO_2 + 2NaOH \rightarrow Na_2SiO_3 + H_2O$$

To prevent the dissolving of the FTO layer and the corresponding glass substrate, the

TiO_2 layer was also annealed at 550^oC to form a firm contact between the TiO_2 and FTO layers. In this case, TiO_2 can serve as a protective layer.

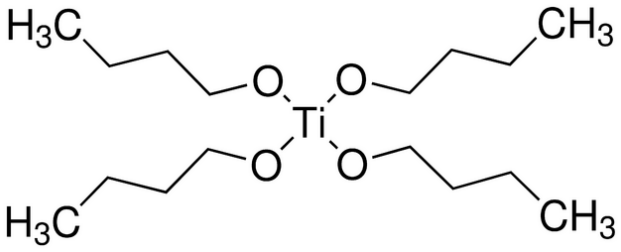

Figure 4-1 molecular structure of Titanium (IV) butoxide

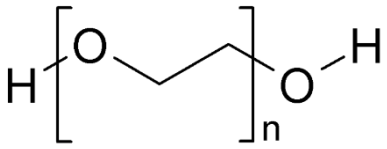

Figure 4-2 molecular structure of PEG

4.2.2 Growing anatase TiO_2 nanowires on an FTO substrate with an anatase TiO_2 overlay layer

Anatase TiO_2 nanowires were grown on FTO substrates with dip-coated anatase TiO_2 overlay layers. First, FTO glass substrates with dip-coated TiO_2 overlay layers

were put into a 23-mL Teflon reactor which contained 10 mL 10 M NaOH aqueous solution, then sealed in a metal bomb. Second, the bomb was moved into an oven and baked at 130-200℃ for several hours.

$$3TiO_2 + 2NaOH \rightarrow Na_2Ti_3O_7 + H_2O$$

Third, after being removed from the Teflon reactor, the samples were moved into a 0.3M HCl aqueous solution to proceed with the ion-exchange process, and then rinsed with DI water.

$$Na_2Ti_3O_7 + 2HCl \rightarrow H_2Ti_3O_7 + 2NaCl$$

To increase the purity of grown anatase TiO_2 nanowires, the above process was repeated several times. Finally, the samples were annealed at 600℃ for two hours at a ramping rate of 1℃/min.

$$H_2Ti_3O_7 \rightarrow 3TiO_2 + H_2O$$

4.3. Fabrication of DSSCs based on anatase TiO_2 nanowires

To illustrate the great potential of longer anatase TiO_2 nanowires for the application of clean energy, DSSCs were fabricated by using the grown anatase TiO_2 nanowires as photoelectrodes.

First, FTO glass substrates with grown anatase nanowires were immersed in N-719 dye (Solaronix Inc., Switzerland) solution (0.3mM ethanol) overnight. Second, the redox electrolyte was prepared by mixing the commercial electrolyte MPN-100 (Solaronix Inc., Switzerland) with acetonitrille (containing 0.1 M LiI) at a ratio of 1:2. Third, 100nm Pt-coated FTO glass substrate was fabricated as the counter electrode. Fourth, the DSSC was constructed with a sandwiched structure by injecting the redox electrolyte between two electrodes. Finally, the performance of the fabricated DSSCs was tested under AM 1.5 spectra illumination with a solar simulator made by Newport Corporation.

4.4. Experimental Results and Discussions

4.4.1 Grown anatase TiO_2 nanowires

According to previous research, $Na_2Ti_3O_7$ nanoflakes or nanowires start to appear on the surface or the edges of TiO_2 nanocrystals or TiO_2 nanoparticles. To ensure a connection between the newly-synthesized nanowires and the TiO_2 nanocrystals, a bulk-like or compacted nanocrystal TiO_2 thin film must be deposited on FTO substrate in advance. The up-to-down synthesis method can also ensure that the TiO_2 bulk-like

thin film connects with the underlying FTO substrate before the transformation occurs at the interface of the TiO_2 thin film and the FTO substrate. To further increase the quality of TiO_2 bulk-like thin film, PEG was added to the dip-coating solution. Without added PEG, the film formed from dip-coating will be discontinuous. The SEM pictures shown in **Fig. 4-3** illustrate the difference between films deposited with and without PEG. **Fig. 4-3 (b)** shows that the TiO_2 bulk-like thin film dip-coated in a solution that included PEG is apparently more compact and continuous than the TiO_2 thin film shown in **Fig. 4-3(a)**, dip-coated in a solution without PEG.

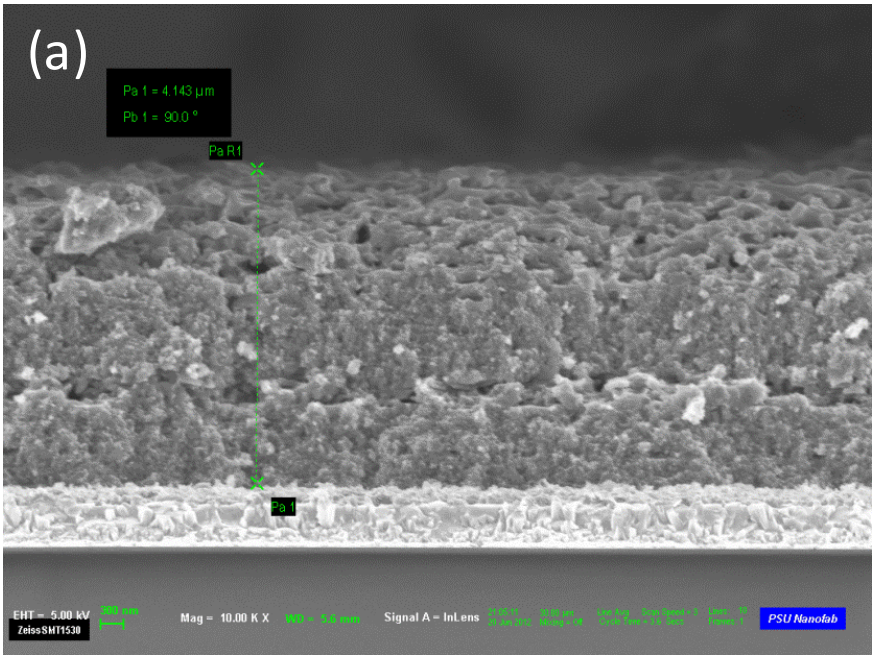

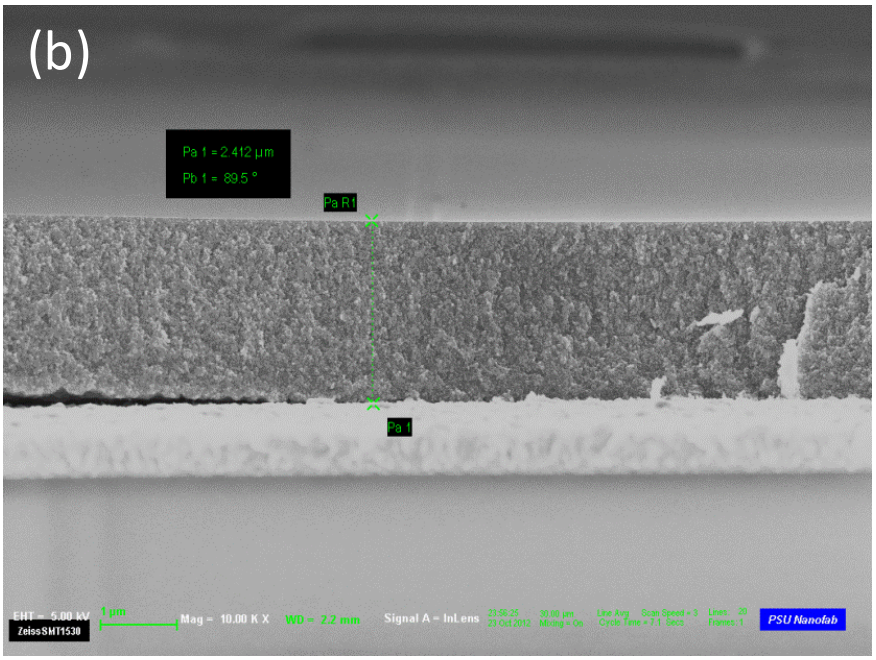

Figure 4-3 (a) The cross-section SEM picture of TiO_2 thin film dip-coated without PEG. (b) The cross-section SEM picture of TiO_2 bulk-like thin film dip-coated with PEG.

By using the method and process described in Section 4.2, anatase TiO_2 nanowires were successfully grown. To illustrate the grown samples at different stages, scanning electron microscope (SEM) pictures for samples at different stages were taken. **Fig. 4-4(a)** shows the SEM picture of grown anatase TiO_2 thin film (~2.5 um) by dip-coating. **Fig. 4-4(b)** shows the SEM picture of the sample after anatase TiO_2 thin film was alkaline-hydrothermally treated in 10M NaOH aqueous solution at 140℃ for two hours. It can be seen that a group of $Na_2Ti_3O_7$ nanoflakes with a thickness of around 1.5um was formed. As the time of the hydrothermal process increases, the shape of the

nanostructure is also changed from a nanoflake shape to a nanowire shape (i.e., thinner and taller). **Fig. 4-4(c)** shows the SEM picture of the sample after three and a half hours of the hydrothermal process. It clearly shows some $Na_2Ti_3O_7$ nanowires, which is consistent with previous reports [12-13]. After ten hours of the hydrothermal process, all the anatase TiO_2 thin film was converted into $Na_2Ti_3O_7$ nanowires, as shown in **Fig. 4-4(d)**.

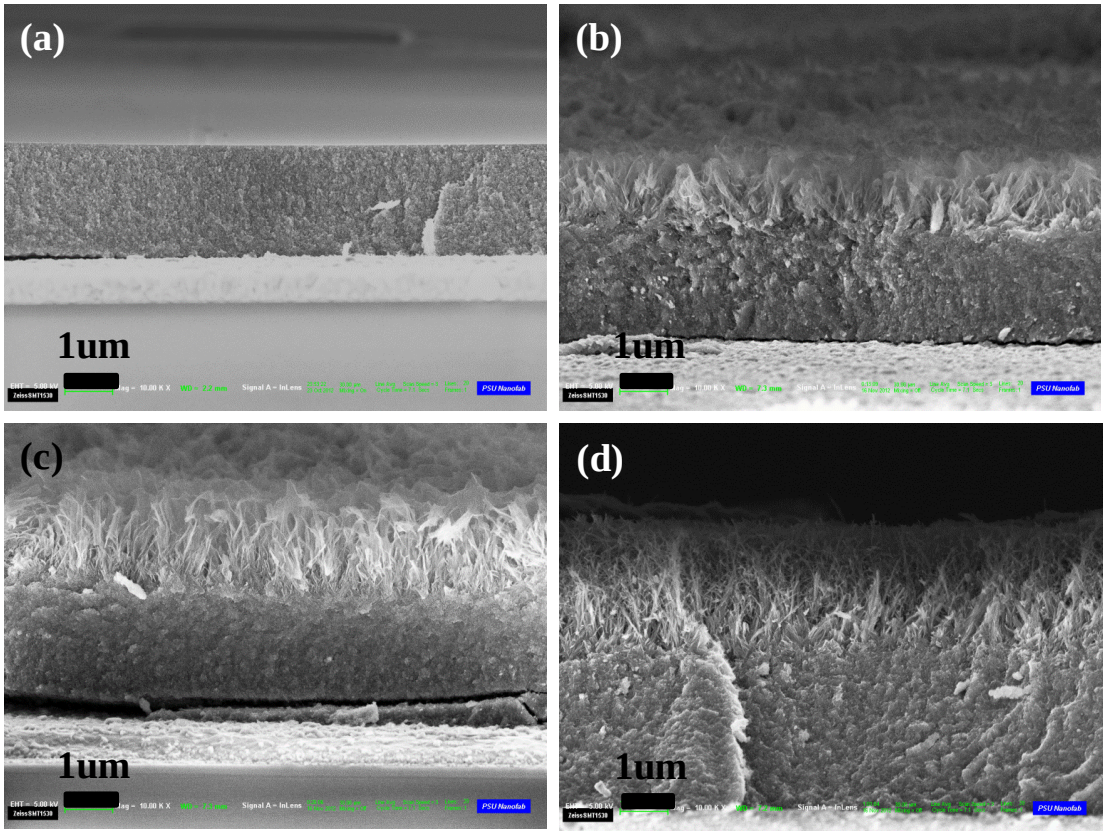

Figure 4-4 (a) An SEM picture of the cross-section of grown anatase TiO_2 thin film by dip-coating, (b) an SEM picture of the cross-section of the sample after alkaline

hydrothermal treatment for two hours, (c) an SEM picture of the cross-section of the sample after alkaline hydrothermal treatment for three and a half hours, and (d) an SEM picture of the cross-section of the sample after alkaline hydrothermal treatment for ten hours.

Finally, as described in Section 4.2, samples were moved into a 0.3M HCl aqueous solution to proceed with the ion-exchange process and then rinsed with DI water. $Na_2Ti_3O_7$ nanowires were converted into anatase TiO_2 nanowires with a similar shape after the ion-exchange and annealing processes, as shown in **Fig. 4-4(d)**.

To verify that the grown nanowires were indeed anatase TiO_2 nanowires, we also conducted x-ray diffraction and transmission electron microscopy (TEM) analyses. First, the XRD chart for the bulk-like TiO_2 thin film grown by the dip-coating method was obtained, as shown in **Fig. 4-5(a)**. The peak locations are at 25.3 $^\circ$, 37.8 $^\circ$, 48.0 $^\circ$, 53.9 $^\circ$, and 55.0 $^\circ$, respectively, which is consistent with the standard XRD pattern of anatase TiO_2 thin film (i.e., JCPDS card number 21-1272). This XRD experimental result confirms that the grown thin film is indeed anatase TiO_2 thin film. Also, the TEM picture shown in **Fig. 4-5(b)** gives the morphology of the anatase bulk-like thin film, showing that it is composited of compact anatase nanocrystals. Second, the XRD chart for the grown $Na_2Ti_3O_7$ nanowires and TiO_2 nanowires was obtained, as shown in **Fig.**

4-5(a). The peak locations of anatase TiO_2 nanowires are at 25.2 ° , 37.7 ° , and 48.0 ° , respectively, which is consistent with the standard XRD spectrum of anatase TiO_2 (i.e., 21-1272). The TEM picture in Fig. 4-5(c) also shows the anatase nanowire is single-crystal. The interplanar spacing of the lattice fringe of nanowire in Fig. 4-5(c) is 3.5Å , corresponding to the peak of the face (101) in **Fig. 4-5(a)**. **Fig. 4-6** shows the anatase nanowires forming during the process of nanoflake splitting. This phenomenon corresponds to the previous research. [4.12-4.13] $Na_2Ti_3O_7$ nanoflakes gradually thicken during the hydrothermal process, resulting in splitting from thick nanoflakes to form thin nanoflakes and nanowires.

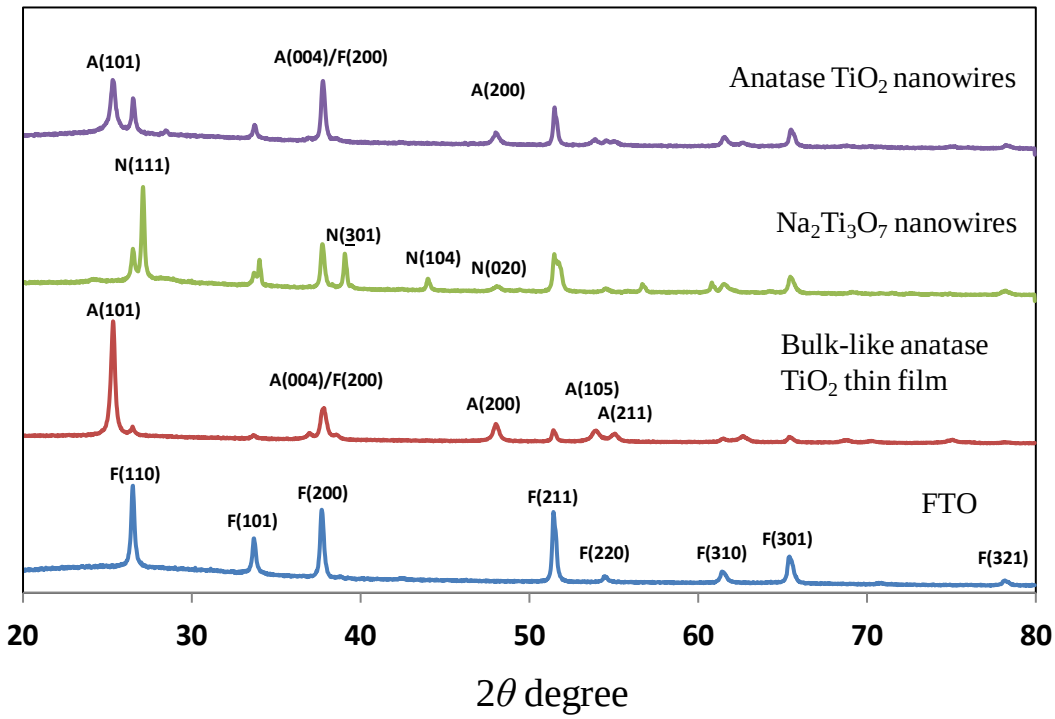

(a)

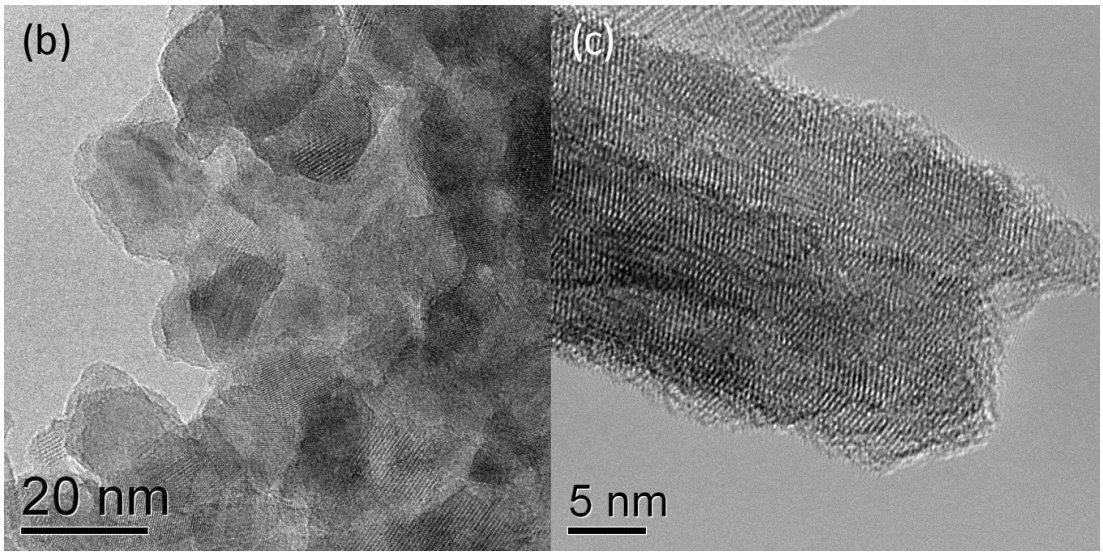

Figure 4-5 (a) XRD patterns of grown samples: blue line: FTO substrate, red line: bulk-like TiO_2 thin film, green line: $Na_2Ti_3O_7$ nanosheets, and pink line: anatase TiO_2 nanowires. (b) The TEM image of TiO_2 bulk-like thin film(c) The TEM image of anatase nanowire in which the periodic lattice fringes show the structure to be single-

crystal.

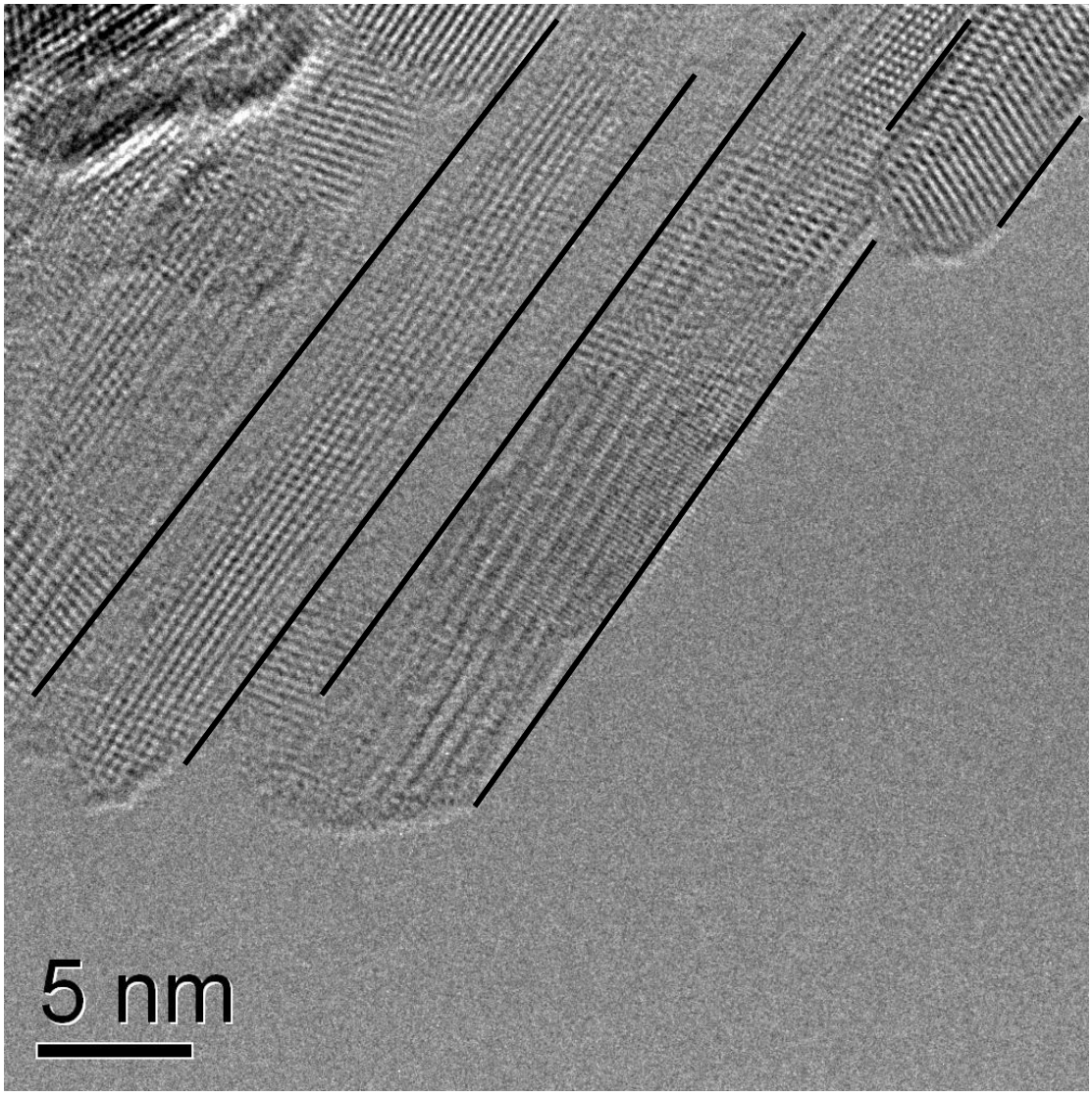

Figure 4-6 Nanowires start to split from nanoflakes.

4.4.2 DSSCs based on the grown TiO_2 nanowires

First, by using the procedures described in Section 4.3., DSSCs based on grown

anatase TiO_2 nanowires with a length of around $2.2\,\mu m$ were fabricated. For comparison purposes, DSSCs based on bulk-like anatase TiO_2 thin film were also fabricated. The performance of the fabricated DSSCs was then evaluated. The blue and red lines of **Fig. 4-7** depict the measured I-V curves of bulk-like anatase TiO_2 thin-film-based DSSCs and anatase TiO_2-nanowire-based DSSCs, respectively. It clearly shows a better I-V curve for the anatase TiO_2-nanowire-based DSSCs. The short-circuit photocurrent density, J_{sc}, the open-circuit voltage (V_{oc}), the fill factor (FF), and light-to-electricity conversion efficiency, (η), for two samples were also measured. The J_{sc}, V_{oc}, FF, and η, for the anatase TiO_2 thin-film-based DSSCs are 2.74 mA/cm^2, 0.73 V, 0.64, and 1.29 percent, respectively. On the other hand, the J_{sc}, V_{oc}, FF, and η, for the anatase TiO_2-nanowire-based DSSCs are 10.64 mA/cm^2, 0.77 V, 0.63, and 5.20 percent, respectively.

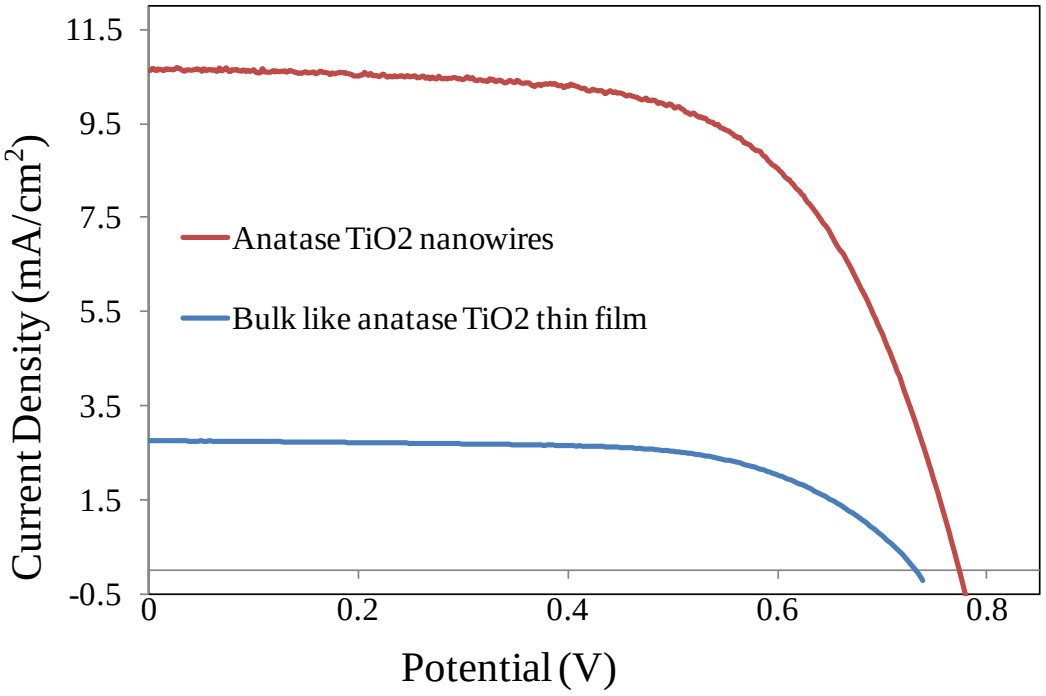

Figure 4-7 The experimentally measured J-V curves of DSSCs based on bulk-like anatase TiO_2 thin film (blue line) and anatase TiO_2 nanowires (red line), respectively.

Both the short-circuit photocurrent density and the light-to-electricity conversion efficiency are much higher (~3.88-fold) in this case, which clearly shows the advantage of using anatase TiO_2 nanowires instead of bulk-like anatase TiO_2 thin film because of the significantly-increased surface area of the former. Another noticeable point is the difference between the open-circuit voltages of these two devices. Open-circuit voltage is basically the difference between the Nernst potential of the redox electrolyte and the Fermi level of the n-type semiconductor (see **Fig. 4-8**). The Fermi level in an n-type semiconductor will be closer to the conduction band of an n-type semiconductor when

more charge is generated in the n-type semiconductor.

$$n \cong N_C e^{\frac{E_f - E_{CB}}{kT}} \tag{4.1}$$

$$N_C = 2\left(\frac{2\pi m_e^* kT}{h^2}\right)^{3/2} \tag{4.2}$$

$$V_{OC} = \frac{E_{CB}}{q} - \frac{E_{CB} - E_f}{q} - \frac{E_{redox}}{q}$$

$$= \frac{E_{CB}}{q} - \left(-kT\, ln \frac{n}{N_C}\right) - \frac{E_{Rredox}}{q}$$

$$= \frac{E_{CB}}{q} + kT\, ln\left(\frac{n}{N_C}\right) - \frac{E_{redox}}{q} \tag{4.3}$$

where n is the density of the electron, N_C is the effective density of states, m_e^* is the electron's effective mass, k is Boltzmann's constant (=8.62×10^{-5}eV/K), h is Planck's constant ($= 6.63 \times 10^{-34}$J − s), E_{CB} is the energy level of the conduction band of TiO_2, and E_{redox} is the Nernst potential of the redox electrolyte.

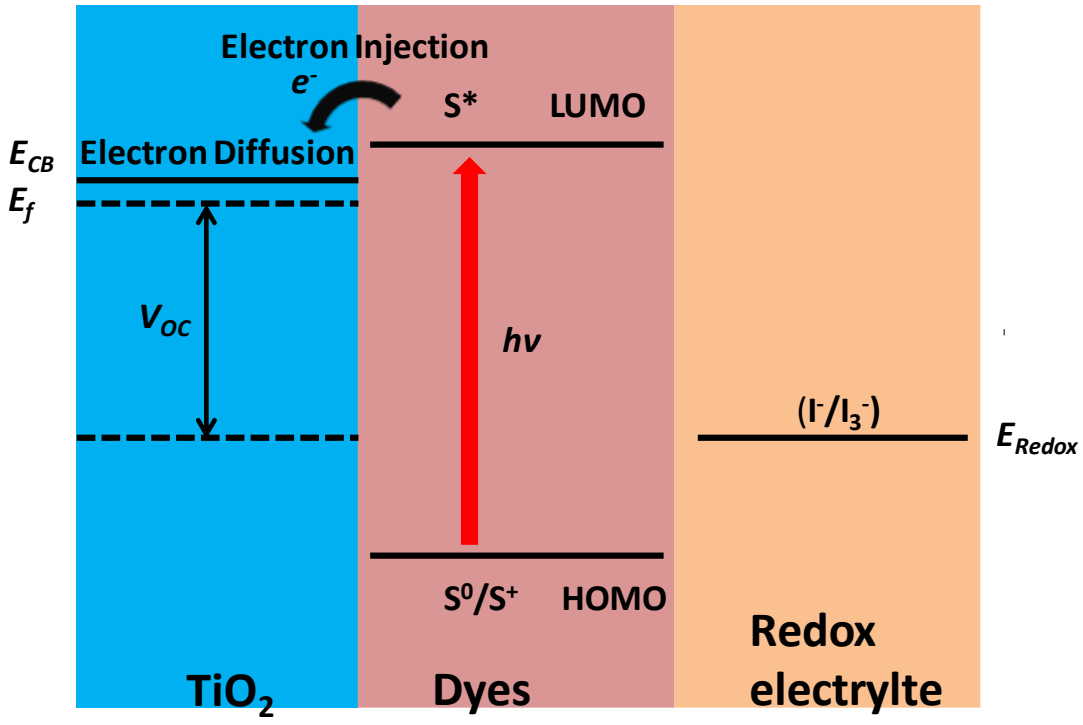

Figure 4-8 V_{oc} is the difference between the Fermi level of TiO_2 and the Nernst potential of the redox electrolyte

Therefore, we can reasonably predict that the charge recombination rate in bulk-like thin-film devices is much higher than that in anatase nanowire devices, resulting in reduction of carriers in the bulk-like thin film. That is to say, charges have better transport ability in anatase nanowires than in bulk-like thin film (composited nanocrystals). Another reason that anatase nanowire solar cells have higher open-circuit voltages than bulk-like thin film solar cells is the size of the nanostructured semiconductor. The diameter of an anatase nanowire in our sample is ~ten nm, which

is much smaller than the thickness of bulk-like thin film (several micro-meters), resulting in less banding of the conduction band. From Eq. 3, this will also increase the difference between the Fermi level of an n-type semiconductor and the Nernst potential (E_{redox}) of a redox electrolyte. **Fig. 4-9** simply illustrates how the conduction bands of different sizes bend at the interface of an electrolyte and an n-type semiconductor. Sizes of structures are represented by **d1**, **d2**, and **d3** (**d1** > **d2** > **d3**). When TiO_2 contacts with redox electrolyte, a Schottky barrier will form at the interface of the n-type semiconductor (TiO_2) and the liquid redox electrolyte. The thickness of the space charge layer in an n-type TiO_2 correlates positively to the size of the TiO_2 [4.14-4.16]. The greater thickness of the space charge layer will cause more bending of the conduction band. In other word, nanowires of smaller size (~ten nanometers) can provide higher open-circuit voltage than bulk-like thin film (~several microns). Furthermore, since the height of our anatase TiO_2 nanowires (~ 2.2 μm) is longer than the one reported in Ref. 9 (~ one μm), the light-to-electricity conversion efficiency of our anatase TiO_2-nanowire-based DSSCs (~5.2 percent) is more than double the efficiency of the DSSCs reported in Ref. 4.9 (~2.1 percent). Again, this represents a substantial advance for the anatase TiO_2-nanowire-based DSSC.

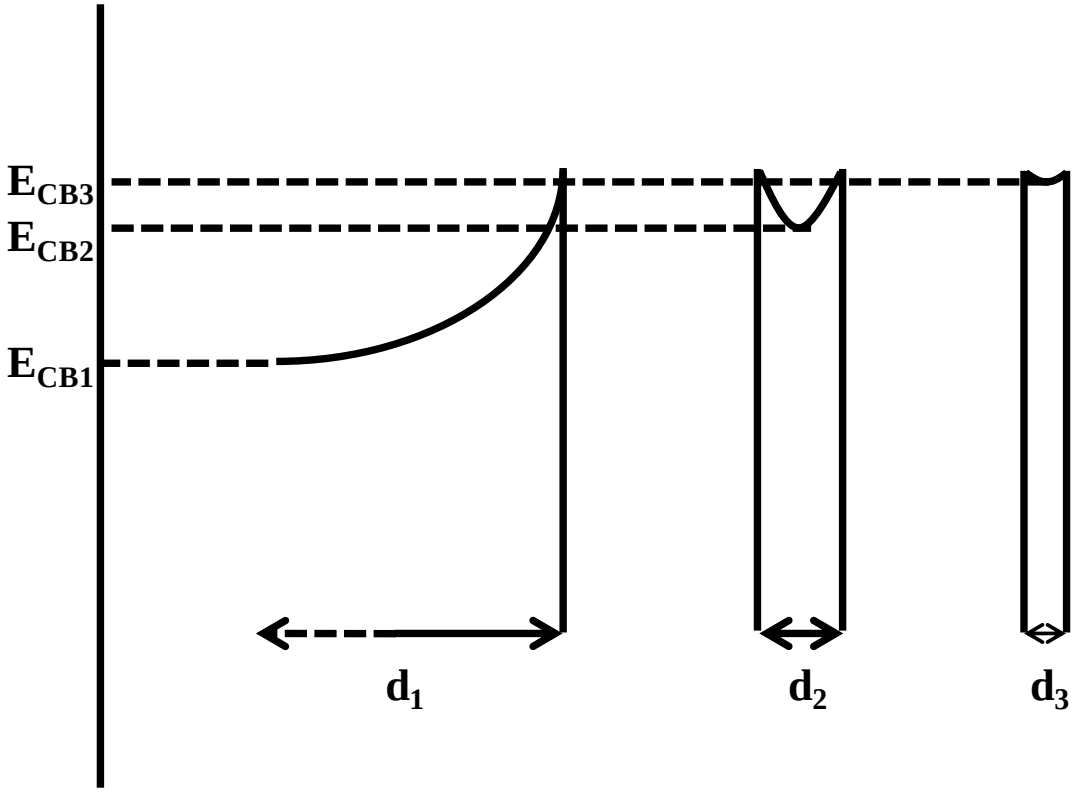

Figure 4-9 The thicker the space charge layer, the more the bending of the conduction band is increased. Therefore, when $d_1 > d_2 > d_3$, then $E_{CB1} < E_{CB2} < E_{CB3}$.

4.5. Conclusion

In conclusion, a new anatase TiO_2-nanowire-growing technique based on a combination of conventional dip-coating and alkaline hydrothermal growth was proposed and demonstrated. The major advantage of this new approach was the capability of growing longer anatase TiO_2 nanowires within a reasonable growing time (e.g. ~ ten hours). A TiO_2 nanowire with a length of around 2.2 μm was successfully

grown, which was more than double the length of the anatase TiO2 nanowire reported in Ref. 4.9. This resulted in a substantial increase in the surface area, which could be beneficial for many clean and renewable energy applications. For example, in terms of DSSCs, the light-to-electricity conversion efficiency based on our TiO_2 nanowire reached 5.2 percent. This was also more than double the light-to-electricity conversion efficiency reported in Ref. 9 and represented a significant technological advance. In the future, we will further refine the technology for growing longer anatase TiO_2 nanowires (e.g. > ten μm) and further improve the light-to-electricity conversion efficiency (e.g. > 20 percent) so that both the cost and the technical performance can better those of current commercial solar cells.

4.6 References

4.1. Brain O'Regan & Michael Grätzel, "A low-cost, high-efficiency solar cell based on dye-sensitized colloidal TiO_2 films," *Nature*, vol. 353, p. 737, 1991.

4.2. M. Law, L. E. Greene, J. C. Johnson, R. Saykally, and P. Yang, "Nanowire dye-sensitized solar cells.," *Nat. Mater.*, vol. 4, no. 6, pp. 455–9, Jun. 2005.

4.3. O. K. Varghese, M. Paulose, and C. a Grimes, "Long vertically aligned titania nanotubes on transparent conducting oxide for highly efficient solar cells.," *Nat. Nanotechnol.*, vol. 4, no. 9, pp. 592–7, Sep. 2009.

4.4. C.-M. Lin, Y.-C. Chang, J. Yao, C. Wang, C. Luo, and S. (Shizhuo) Yin, "Multi-step hydrothermally synthesized TiO_2 nanoforests and its application to dye-sensitized solar cells," *Mater. Chem. Phys.*, vol. 135, no. 2–3, pp. 723–727, Aug. 2012.

4.5. A. F. and K. Honda, "Electrochemical Photolysis of Water at a Semiconductor Electrode," *Nature*, vol. 238, pp. 37–38, 1972.

4.6. J. H. Park, S. Kim, and A. J. Bard, "Novel carbon-doped TiO_2 nanotube arrays with high aspect ratios for efficient solar water splitting.," *Nano Lett.*, vol. 6, no. 1, pp. 24–8, Jan. 2006.

4.7. X. Feng, K. Shankar, O. K. Varghese, M. Paulose, T. J. Latempa, and C. a Grimes, “Vertically aligned single crystal TiO_2 nanowire arrays grown directly on transparent conducting oxide coated glass: synthesis details and applications.,” *Nano Lett.*, vol. 8, no. 11, pp. 3781–6, Nov. 2008.

4.8. B. Liu and E. S. Aydil, “Growth of oriented single-crystalline rutile TiO(2) nanorods on transparent conducting substrates for dye-sensitized solar cells.,” *J. Am. Chem. Soc.*, vol. 131, no. 11, pp. 3985–90, Mar. 2009.

4.9. B. Liu, A. Khare, and E. S. Aydil, “Synthesis of single-crystalline anatase nanorods and nanoflakes on transparent conducting substrates.,” *Chem. Commun. (Camb).*, vol. 48, no. 68, pp. 8565–7, Sep. 2012.

4.10. T. Kasuga, M. Hiramatsu, a Hoson, T. Sekino, and K. Niihara, “Titania Nanotubes Prepared by Chemical Processing,” *Adv. Mater.*, vol. 11, no. 15, pp. 1307–1311, 1999.

4.11. T. Kasuga, M. Hiramatsu, A. Hoson, T. Sekino, and K. Niihara, “Formation of Titanium Oxide Nanotube,” *Langmuir*, vol. 14, no. 12, pp. 3160–3163, Jun. 1998.

4.12. J. Huang, Y. Cao, Q. Huang, H. He, Y. Liu, W. Guo, and M. Hong, "High-Temperature Formation of Titanate Nanotubes and the Transformation Mechanism of Nanotubes into Nanowires," *Cryst. Growth Des.*, vol. 9, no. 8, pp. 3632–3637, Aug. 2009.

4.13. D. Wu, J. Liu, X. Zhao, A. Li, Y. Chen, and N. Ming, "Sequence of Events for the Formation of Titanate Nanotubes , Nanofibers, Nanowires, and Nanobelts.," no. 10, pp. 547–553, 2006

4.14. Z. Zhang, "Enhancing the Open-Circuit Voltage of Dye-Sensitized Solar Cells : CoadSorbents and Alternative Redox Couples," *Thesis*, vol. 4066, 2008.

4.15. M. Kaneko, H. Ueno, and J. Nemoto, "Schottky junction/ohmic contact behavior of a nanoporous TiO(2) thin film photoanode in contact with redox electrolyte solutions.," *Beilstein J. Nanotechnol.*, vol. 2, pp. 127–34, Jan. 2011.

4.16. A. J. Cowan and J. R. Durrant, "Long-lived charge separated states in nanostructured semiconductor photoelectrodes for the production of solar fuels.," *Chem. Soc. Rev.*, vol. 42, no. 6, pp. 2281–93, Mar. 2013.

Chapter 5
Conclusion and Future Directions

5.1 Conclusion

In this dissertation, we analyzed the mechanism of dye-sensitized solar cells and concluded several novel approaches for the future development of dye-sensitized solar cells. One is to develop new a photon sensitizer, dye, which has wider light absorption spectrum (near the IR region) and excellent electronic coupling properties with the n-type semiconductor (photoelectrode). Another approach was the development of new nanostructured n-type semiconductors which could provide large dye attachment surfaces for and a good charge transport pathway for the photo-generated carriers. The three-dimensional TiO_2 nanotree was successfully synthesized on FTO substrate, which providing a greater surface area for dye attachment on small-diameter nanowires (branches) and excellent charge transport pathways with large-diameter nanorods (trunks). By the use of a multi-step hydrothermal method, the dimensions of the nanoforest can be well controlled. An increase in the thickness of the nanoforest and a reduction in fabrication time can be realized and modified from the reported method in

Chapter Three. According to various researches, another TiO_2 phase, anatase, can provide a much better charge diffusion coefficient than the rutile phase. Therefore, we also developed a novel method to synthesize single-crystal anatase nanowires on FTO substrates. The use of a higher open-circuit voltage illustrated that charge recombination could be greatly decreased with the anatase nanowire-synthesized FTO substrate.

5.2 Photoelectrochemical water-splitting devices

Besides its use in dye-sensitized solar cells, TiO_2 also plays an important role in photo-electrochemical water-splitting devices because TiO_2 has the properties of stability, proper band position, high band gap (>1.23eV), and good conductivity. However, the traditional water-splitting devices based on TiO_2 photoelectrodes have low conversion efficiency due to two main reasons: 1. TiO_2 cannot absorb all of the visible light and even light from the IR region of the spectrum because the band gap of TiO_2 is ~3.2eV; 2. The rapid recombination of photo-excited electron/hole pairs. Many techniques, such as chemical additives for H_2 production enhancement and photo-catalyst modification techniques, have been developed to improve water-

splitting efficiency in recent years. [5.1-5.6]

$$TiO_2 \xrightarrow{hv} e^-_{TiO_2} + h^+_{TiO_2}$$

Among these different methods, dye sensitization is largely adopted to enhance energy conversion in the visible and IR regions of the spectrum. Our developed nanostructured materials, 3-D TiO_2 nanoforests and 1-D single-crystal anatase nanowires, have great potential for application in dye-sensitized water-splitting devices. The properties of large surface area and good charge-diffusion ability match the qualifications for photoelectrodes used in water-splitting devices.

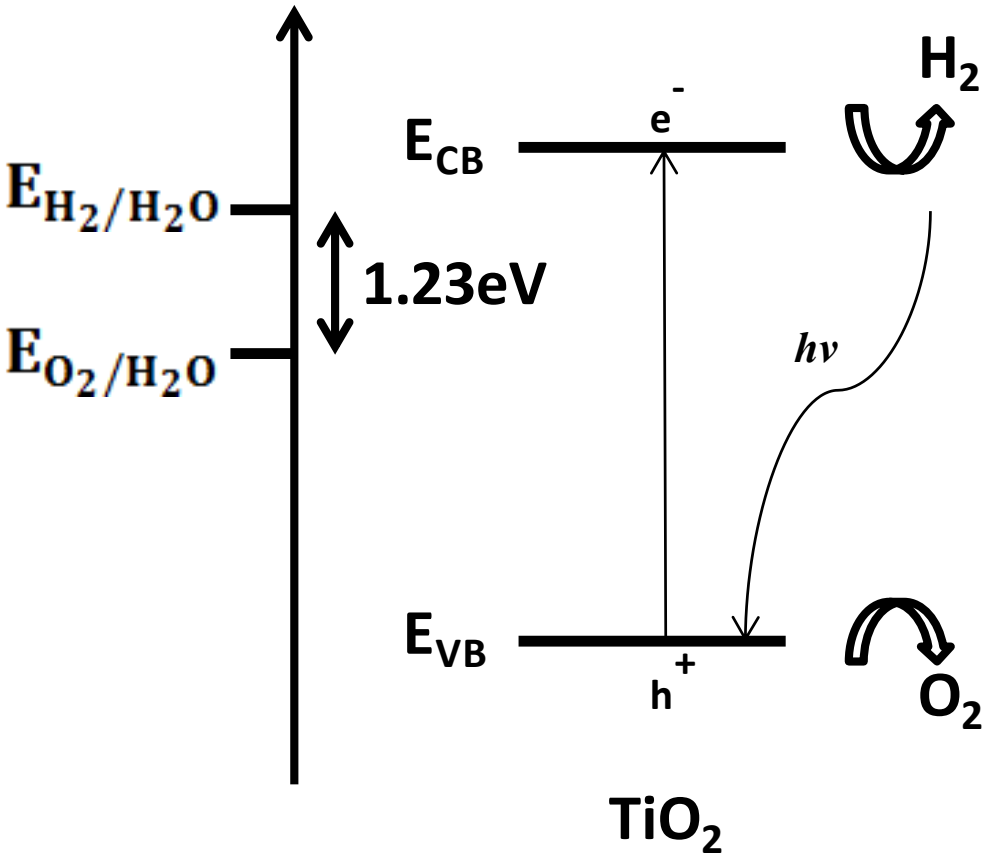

Figure 5-1 The traditional mechanism of photocatalytic water splitting. With excitation of the photon (*hv*), an electron/hole pair is generated. The electron and hole can migrate to the surface of TiO_2 and reduce and oxidize the reactants absorbed by TiO_2. Hydrogen and oxygen can be produced through this process.

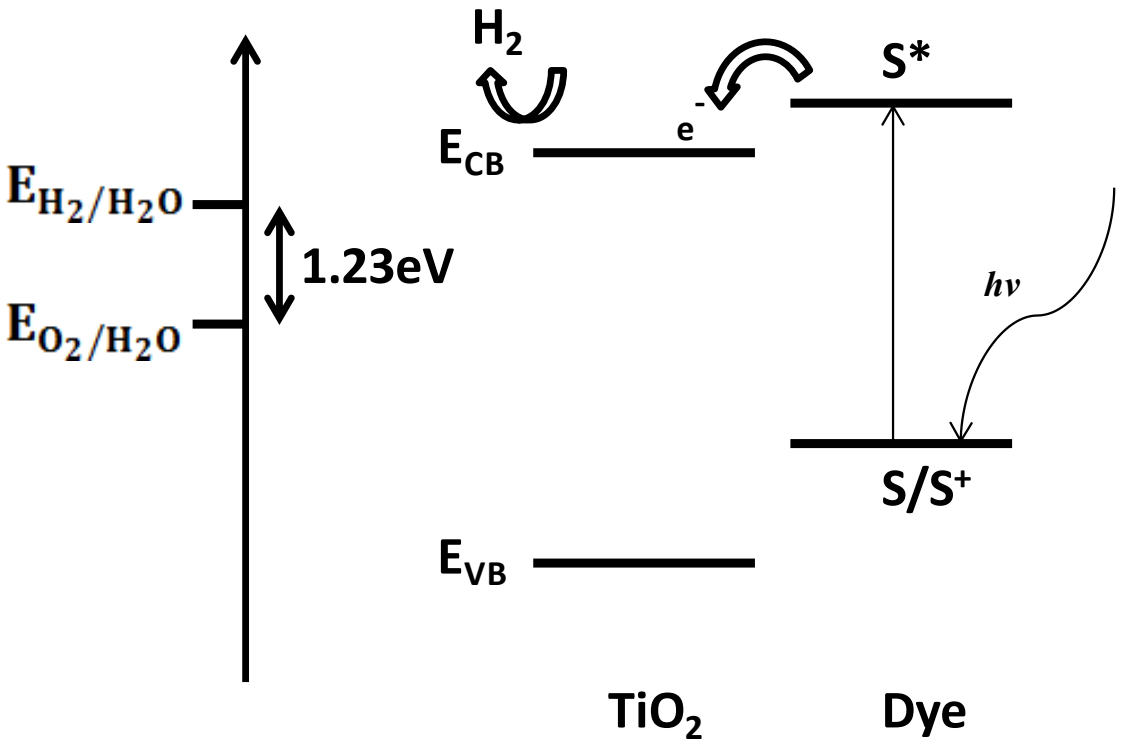

Figure 5-2 Water-splitting device with dye sensitization. The dye can absorb the photon of energy (<3.2eV), so that more electron/hole pairs can be generated. Electrons will be injected into TiO_2, where they will react with the reactants at the surface of the TiO_2 to produce hydrogen.

5.3 Hydrogen detection

To decrease the impacts of fossil fuel usage on the environment, hydrogen, one of the most important clean energy sources, has attracted much attention. In the previous paragraph, we have illustrated how hydrogen can be produced from utilization of another clean energy technology, solar power, based on our developed materials.

Hydrogen detection is another important category in the development of hydrogen utilization. Titanium dioxide is a very good semiconductor material for hydrogen detection due to its high stability and high electronic sensitivity to hydrogen. [5.7-5.11] The mechanism of hydrogen detection based on a TiO_2 electrode is the chemisorption of hydrogen atoms on the surface of TiO_2 nanostructures, resulting in the separation of hydrogen ions (H^+) and electrons (e^-) and the accumulation of electrons at the surface of the TiO_2. Due to the accumulation of electrons, the conductivity of the TiO_2 nanostructures increases. Therefore, when an electrical field is fed across the TiO_2 nanostructures (nanowires or nanoforests), the current across the nanostructures will be greater with exposure to hydrogen gas than without it.

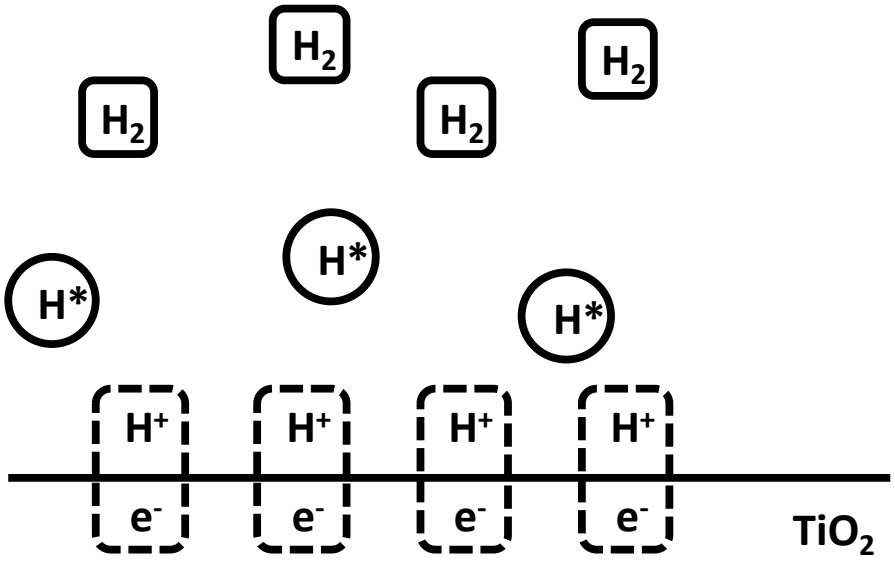

Figure 5-3 The chemisorption of spilled-over hydrogen atoms at the surface of TiO_2 makes hydrogen ions and electrons partially separate. The accumulation of electrons makes the conductivity of TiO_2 increase.

The transient response pattern and the sensitivity (S) are the two indices to determine the performance of the hydrogen gas sensor. The sensitivity can be defined as:

$$S = \frac{I_G - I_O}{I_O}$$

where I_G is the current after the sensor is exposed to H_2, and I_O is the current when the sensor is exposed without H_2.

We plan to further adapt our developed materials, single-crystal anatase nanowires and rutile nanoforests, for hydrogen gas detection. Advanced research, such as doping and modifying the geometry of the nanostructured thin films, will be undertaken to improve performance. **Fig. 5-4** shows the schematic diagram of a hydrogen gas sensor based on TiO_2 nanostructures (nanoforests/nanowires).

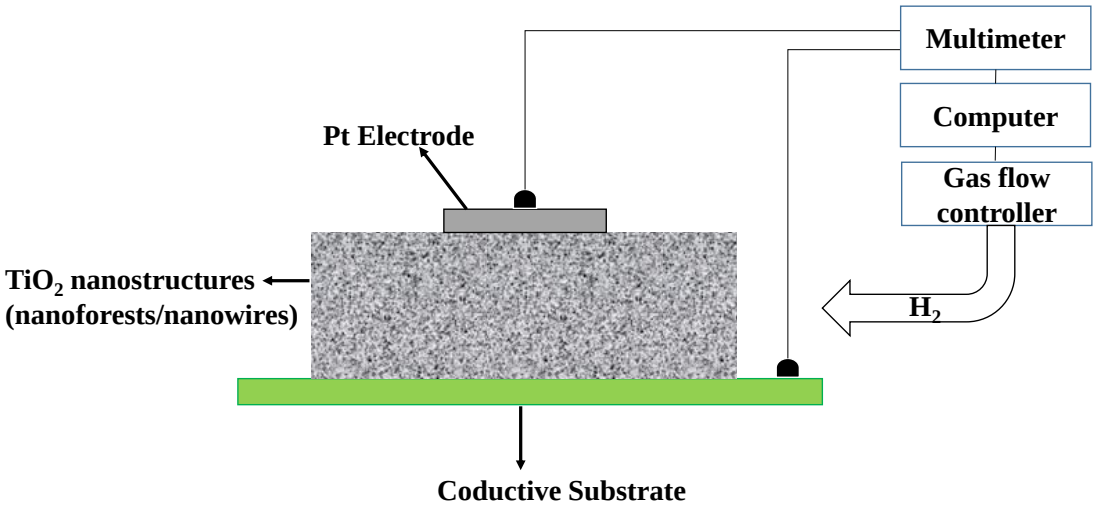

Figure 5-4 Schematic diagram of a hydrogen gas sensor

5.4 Supercapacitors

Research on supercapacitors has been thoroughly researched because of their properties of high capacitance per unit volume and great energy density. In recent years, there have been considerable advances in supercapacitors because of the well-developed nanostructure metal oxide, which can be used as the electrode of the supercapacitor [5.12-5.17]. It has been proven that nanostructured TiO_2 plays an important role in supercapacitors due to its high charge-transport ability and high surface area for interaction with redox electrolyte. We believe that the 1-D single-crystal nanowires and 3-D TiO_2 nanoforests described in this thesis have great potential for application to

supercapacitors in the future.

5.5 References

5.1. P. Szymanski and M. a. El-Sayed, “Some recent developments in photoelectrochemical water splitting using nanostructured TiO_2: a short review,” *Theor. Chem. Acc.*, vol. 131, no. 6, p. 1202, May 2012.

5.2. J. R. Swierk and T. E. Mallouk, “Design and development of photoanodes for water-splitting dye-sensitized photoelectrochemical cells.,” *Chem. Soc. Rev.*, vol. 42, no. 6, pp. 2357–87, Mar. 2013.

5.3. Y. Zhao, J. R. Swierk, J. D. Megiatto, B. Sherman, W. J. Youngblood, D. Qin, D. M. Lentz, A. L. Moore, T. a Moore, D. Gust, and T. E. Mallouk, “Improving the efficiency of water splitting in dye-sensitized solar cells by using a biomimetic electron transfer mediator.,” *Proc. Natl. Acad. Sci. U. S. A.*, vol. 109, no. 39, pp. 15612–6, Sep. 2012.

5.4. J. Brillet, J. Yum, M. Cornuz, T. Hisatomi, R. Solarska, J. Augustynski, M. Graetzel, and K. Sivula, “Highly efficient water splitting by a dual-absorber tandem cell,” *Nat. Photonics*, vol. 6, no. December, pp. 2–6, 2012.

5.5. M. G. Walter, E. L. Warren, J. R. McKone, S. W. Boettcher, Q. Mi, E. a Santori, and N. S. Lewis, “Solar water splitting cells.,” *Chem. Rev.*, vol. 110,

no. 11, pp. 6446–73, Nov. 2010.

5.6. M. Ni, M. K. H. Leung, D. Y. C. Leung, and K. Sumathy, “A review and recent developments in photocatalytic water-splitting using TiO_2 for hydrogen production,” *Renew. Sustain. Energy Rev.*, vol. 11, no. 3, pp. 401–425, Apr. 2007.

5.7. U. Roland, R. Salzer, T. Braunschweig, F. Roessner, and H. Winkler, “Investigations on Hydrogen Spillover,” *J. CHEM. SOC. FARADAY TRANS.*, vol. 91, no. 7, pp. 1091–1095, 1995.

5.8. Z. Li, D. Ding, and C. Ning, “p-Type hydrogen sensing with Al- and V-doped TiO_2 nanostructures.,” *Nanoscale Res. Lett.*, vol. 8, no. 1, p. 25, Jan. 2013.

5.9. O. K. Varghese, D. Gong, M. Paulose, K. G. Ong, E. C. Dickey, and C. a. Grimes, “Extreme Changes in the Electrical Resistance of Titania Nanotubes with Hydrogen Exposure,” *Adv. Mater.*, vol. 15, no. 78, pp. 624–627, Apr. 2003.

5.10. S. K. Hazra and S. Basu, “High sensitivity and fast response hydrogen sensors based on electrochemically etched porous titania thin films,” *Sensors Actuators B Chem.*, vol. 115, no. 1, pp. 403–411, May 2006.

5.11. Z. Li, D. Ding, Q. Liu, and C. Ning, “Hydrogen sensing with Ni-doped TiO_2 nanotubes.,” *Sensors (Basel).*, vol. 13, no. 7, pp. 8393–402, Jan. 2013.

5.12. M. Salari, S. H. Aboutalebi, K. Konstantinov, and H. K. Liu, “A highly ordered titania nanotube array as a supercapacitor electrode.,” *Phys. Chem. Chem. Phys.*, vol. 13, no. 11, pp. 5038–41, Mar. 2011.

5.13. C. Bian, A. Yu, and H. Wu, “Fibriform polyaniline/nano-TiO_2 composite as an electrode material for aqueous redox supercapacitors,” *Electrochem. commun.*, vol. 11, no. 2, pp. 266–269, Feb. 2009.

5.14. X. Lu, M. Yu, G. Wang, T. Zhai, S. Xie, Y. Ling, Y. Tong, and Y. Li, “H-TiO(2) @MnO(2) //H-TiO(2) @C core-shell nanowires for high performance and flexible asymmetric supercapacitors.,” *Adv. Mater.*, vol. 25, no. 2, pp. 267–72, Jan. 2013.

5.15. X. Lu, G. Wang, T. Zhai, M. Yu, J. Gan, Y. Tong, and Y. Li, “Hydrogenated TiO_2 nanotube arrays for supercapacitors.,” *Nano Lett.*, vol. 12, no. 3, pp. 1690–6, Mar. 2012.

5.16. K. Xie, J. Li, Y. Lai, Z. Zhang, Y. Liu, G. Zhang, and H. Huang, “Polyaniline nanowire array encapsulated in titania nanotubes as a superior electrode for

supercapacitors.," *Nanoscale*, vol. 3, no. 5, pp. 2202–7, May 2011.

5.17. R. B. Ambade, S. B. Ambade, N. K. Shrestha, Y.-C. Nah, S.-H. Han, W. Lee, and S.-H. Lee, "Polythiophene infiltrated TiO_2 nanotubes as high-performance supercapacitor electrodes.," *Chem. Commun. (Camb).*, vol. 49, no. 23, pp. 2308–10, Mar. 2013.

Vita

Education:

PhD, Electrical Engineering,The Pennsylvania State University , PA,2014

MS, Electrical Engineering and Computer Science, Northwestern University, IL, December 2006

MS, Electrical Engineering, National Taiwan University, Taiwan, June 2002

BS, Electrical and Control Engineering, National ChiaoTung University, Taiwan, June 2000

Journal Publications:

- **Chih-Min Lin**, Yun-Ching Chang, Jimmy Yao, Chao Wang, Claire Luo, and Stuart (Shizhuo) Yin, "Multi-step hydrothermally synthesized TiO2 nanoforests and its application to dye-sensitized solar cells", *Materials Chemistry and Physics*.,**135**, 723(2012)
- Yun-Ching Chang, **Chih-Min Lin**, Jimmy Yao, Chao Wang, and Stuart Yin, "Field induced dynamic waveguides based on potassium tantalate niobate crystals", *OPTICS EXPRESS*., **20**, 21128(2012)
- Zhong Li, Karthik Shankar, Gopal K. Mor, Robert A. Grimminger, **Chih-Min Lin**, John E. Anthony, and Craig A., "Grimes,Functionalized pentacenes for dye-sensitized solar cells", *Journal of Photonics for Energy*.,**1**, 011106-2(2011)

Conference Publications:

- **Chih-Min Lin**, and Shizhuo Yin, "High aspect ratio titania 3-dimension (TiO2) nanostructures:Fabrication and Applications." SPIE, San Diego, USA (2012)
- Chao Wang, **Chih-Min Lin**, Shizhuo Yin, "Black silicon created by interfered femtosecond laser illumination." SPIE, San Diego, USA (2012)
- **Chih-Min Lin**, Jen Sloppy, Xinjian Feng, and Craig A. Grimes, "Highly Oriented Anatase Nanowire Arrays on Transparent Conducting Oxide Substrates for DSSC Application," Mallorca, Spain (2010)
- Karthik Shankar, Zhong Li, Oomman Varghese, Xinjian Feng, **Chih-Min Lin**, John E. Anthony and Craig A. Grimes, **"**Hybrid Solar Cells from Vertically Oriented TiO2 Nanotube/Nanowire Arrays and Soluble Functionalized Linear Acenes**."** 2009 MRS Fall Meeting, Boston, USA (2009)
- Karthik Shankar, Gopal K Mor, **Chih-Min Lin**, Oomman K Varghese, Maggie Paulose and Craig A Grimes**, "**Titania Nanotube Array Based Large Area Polymeric and Dye-Sensitized Solar Cells.**"** 2008 MRS Fall Meeting, Boston, USA (2008)